

MASARYKOVA UNIVERZITA

Přírodovědecká fakulta

Ústav teoretické fyziky a astrofyziky

BAKALÁŘSKÁ PRÁCE

**Modelování interakcí hvězd s okolní látkou v blízkosti
Galaktického centra**

Georgii Bless

Vedoucí bakalářské práce: Mgr. Ing. arch. Petr Kurfürst, Ph.D.

2025

Bibliografický záznam

Autor: Georgii Bless
Přírodovědecká fakulta
Masarykova univerzita
Ústav teoretické fyziky a astrofyziky

Název práce: Modelování interakcí hvězd s okolní látkou
v blízkosti Galaktického centra

Studijní program: Fyzika

Studijní obor: Astrofyzika

Vedoucí práce: Mgr. Ing. arch. Petr Kurfürst, Ph.D

Akademický rok: 2024/2025

Počet stran: VIII + 43

Klíčová slova: Akreční disk, supernovy, hydrodynamika, numerické modely,
Castro, AMR, SNEC, Sedona

Bibliographic Entry

Author: Georgii Bless
Faculty of Science
Masaryk University
Department of Theoretical Physics and Astrophysics

Title of the Thesis: Modeling stellar interactions with the surrounding material
near the Galactic Centre

Degree Programme: Physics

Field of Study: Astrophysics

Supervisor: Mgr. Ing. arch. Petr Kurfürst, Ph.D

Academic Year: 2024/2025

Number of Pages: VIII + 43

Keywords: Accretion disk, supernovae, hydrodynamics, numerical models,
Castro, AMR, SNEC, Sedona

Acknowledgments

First of all I would like to thank Mgr. Ing. arch. Petr Kurfürst, Ph.D, for giving me all the necessary knowledge, patience and time. My work with him on this thesis greatly enhanced my knowledge and experience, and I couldn't have wished for a better supervisor.

Also, I wouldn't want to forget the tremendous cheering and love from my family and friends. I owe my survival over the last four years to them.

Declaration

I declare that I have prepared my Bachelor's thesis independently under the supervision of the thesis supervisor using the information sources cited in the thesis

Brno 13.05.2025

.....

Georgii Bless

Abstrakt:

Tato práce se zabývá explozemi supernov (SN) v blízkosti Galaktického centra (GC) a jejich interakcemi s okolní látkou. V blízkosti GC se nachází hodně struktur hustého plynu a v této práci byly použity především akreční disky. Pomocí numerických kódů, hydrodynamických a radiačních výpočtů porovnááme rozdíly mezi izolovanými explozemi SN a těmi s galaktickým akrečním diskem v blízkosti. Profily SN po průrazu rázové vlny byly generovány pomocí kódu SuperNova Explosion Code (SNEC) a později použity ve vícerozměrných simulacích s kódem Castro. Ten je určen pro simulaci stlačitelných astrofyzikálních toků a má implementovanou techniku Adaptive Mesh Refinement. Ze simulované exploze SN a její interakce s akrečním diskem následně vypočítal kód přenosu záření Sedona, který je založen na algoritmu Monte Carlo, některé světelné křivky, které pak byly porovnané s jinými modely a pracemi.

Abstract:

This work discusses supernovae (SN) explosions near the Galactic Center (GC) and their interactions with surrounding material. There are many dense gaseous structures closely to GC, and the primarily used ones in this work were Galactic accretion disk. Using numerical codes for hydrodynamics and radiation calculations, we compare the difference between isolated SN explosion, and those with Galactic accretion disk nearby. Post shock wave breakout SN profiles were generated by the SuperNova Explosion Code (SNEC) and later used in multi-dimensional simulations with Castro code. It is designed for simulating compressible astrophysical flows, with implemented Adaptive Mesh Refinement technique. From simulated SN explosion and interaction with accretion disk, the radiation-transfer Sedona code, which is based on the Monte Carlo algorithm, calculated some light curves which were compared to different models and studies.

ZADÁNÍ
BAKALÁŘSKÉ PRÁCE

Akademický rok: 2024/2025

Ústav:	Ústav teoretické fyziky a astrofyziky
Student:	Georgii Bless
Program:	Fyzika
Specializace:	Astrofyzika

Ředitel ústavu PŘF MU Vám ve smyslu Studijního a zkušebního řádu MU určuje bakalářskou práci s názvem:

Název práce:	Modelování interakcí hvězd s okolní látkou v blízkosti Galaktického centra
Název práce anglicky:	Modelling stellar interactions with the surrounding material near the Galactic Centre
Jazyk práce:	angličtina

Oficiální zadání:

There are a number of formations around galactic centres. In addition to the supermassive black holes at the very centre and the large number of stars in the nuclear star cluster, these can include the central accretion disk, the associated gas dust torus, the galactic jet, regions of broad or narrow spectral lines, and so on. It is the number of stars in a nuclear star cluster that increases the frequency of their interactions with the surrounding interstellar material. The manifestations of such interactions can be extremely interesting from an observational and theoretical point of view and can yield a wealth of insights. To understand their meaning, the physics of these interactions needs to be modelled and the results of such models need to be compared with observed data. The task of this bachelor thesis will be to model some types of interactions, such as the passage of a star through a galactic disk and its manifestations as a function of the inclination angle of the star's orbit with respect to the disk or the processes that take place in the torus, the broad lines region, etc.

Literatura:

BINNEY, James a Scott TREMAINE. *Galactic dynamics*. 2nd ed. Princeton: Princeton University Press, 2008, xvi, 885. ISBN 9780691130279.

Vedoucí práce:	Mgr. Ing. arch. Petr Kurfürst, Ph.D.
Konzultant:	RNDr. Michal Zajaček, Dr. rer. nat.
Datum zadání práce:	18. 10. 2024
V Brně dne:	13. 5. 2025

Zadání bylo schváleno prostřednictvím IS MU.

Georgii Bless, 18. 10. 2024

Mgr. Ing. arch. Petr Kurfürst, Ph.D., 20. 10. 2024

RNDr. Luboš Poláček, 4. 12. 2024

Contents

1	The Galactic Center	2
1.1	Introduction	3
1.2	Galactic coordinate system	4
1.3	General structure	6
1.4	Central Molecular Zone	6
1.5	Nuclear Star Cluster	7
2	Supernovae and their explosions	9
2.1	Classification of supernovae	9
2.1.1	Type I SNe	9
2.1.2	Type II SNe	10
2.2	Explosions and interactions	13
2.2.1	Riemann-Sod shock tube	13
3	Astrophysical programs and codes	15
3.1	SNEC	15
3.1.1	Equations	15
3.1.2	Equations of state and numerical scheme	17
3.2	Castro	17
3.2.1	Adaptive mesh refinement	18
3.2.2	Hydrodynamics	18
3.2.3	EOS	19
3.2.4	Radiation	19
3.3	Sedona	20
3.4	MetaCentrum	21

4 Models **22**

4.1 Isolated supernova 23

4.2 SN surroundings, disk model 25

4.3 Calculated models 27

4.4 Calculated light curves 35

4.5 Discussion 36

Introduction

The Galactic Center offers a very unique environment for numerical modeling, with a supermassive black hole surrounded by a lot of gas and a dense stellar cluster. This work will try to describe the Galactic Center, supernovae explosions and their interactions with surrounding material. After that, we discuss some of the models.

It is divided into 4 chapters, with first two being the theoretical part of this work. First, we will look and discuss the Galactic Center, mainly its structure and environment. The next theoretical chapter briefly describes some of the supernovae classification, core-collapse mechanism, and some relevant and well understood phenomena that happen after explosion (e.g., the Riemann-Sod shock tube problem).

Next two chapters are the practical part of this work. The first one will describe tools which were used in this work. Here we will look at used astrophysical codes, their physics and some numerical methods. After that, in Chapter 4, we discuss our own models. Their solutions, differences, generated light curves, and some numerical complications that occurred. After that, we compare the results with some known studies and suggest the conclusions.

Chapter 1

The Galactic Center

Gravity acts as the binding force for galaxies, which are composed of stars, planets, extensive nebulae of gas, and the dark matter. While galaxies exhibit a variety of forms, they are primarily categorized as spiral or elliptical, with less common, oddly formed types known as irregular. The term **galaxy** originates from the Greek term *galaxías*, whose literal translation is 'milky'. This name arose from the initial visual impression of the Milky Way as a luminous, milky strip across the night sky. It wasn't known until 1610 that Galileo Galilei, through his telescopic observations, provided evidence that our Galaxy, the Milky Way, is comprised of numerous stars. Following this discovery, understanding of our galaxy progressively grew, with Immanuel Kant offering an accurate explanation of the gravitational forces binding it together in his work *Universal Natural History and Theory of the Heavens* (1755). In 1918, Harlow Shapley proposed that the halo of globular clusters encircling the Milky Way appeared to be centered on the stellar concentrations within the Sagittarius constellation (see Shapley, 1918), but thick molecular clouds prevented optical astronomy from peering into the center. From the 1950s onward, astronomers became aware of an exceptionally potent radio wave source radiating from the Galactic Center's direction. It was only in 1968 that Eric E. Becklin and Gerald Neugebauer succeeded in observing the central parsecs of the Galaxy using infrared wavelengths (see Sanders and Wrixon, 1974). Their findings revealed incredibly concentrated clusters of stars, possessing star density a million times greater than in the vicinity of our Solar System. These extraordinary properties make the Galactic Center a very unique environment. Being a very popular target since 1960s, it still attracts a lot of attention from observatories and researchers from around the world.

1.1 Introduction

Galactic Center, due to its large concentration of stars and gas provides an exclusive 'laboratory' for studying astrophysical processes based on mutual interactions of either stellar bodies or stars and surrounding gas forming circumstellar matter. Even the gaseous structures near the Galactic Center, especially within the Nuclear Star Cluster, are significantly more abundant with mostly denser gas and dust distribution. This is the case of the central Galactic accretion disk surrounded by gas-dust torus. Studying interactions of SNe or, for example, the Galactic jet (which was active in the past in our Galaxy) with these structures provide very important source of information about evolution of stars and circumstellar medium.

The abundance of gas and dust in the Galactic plane results in about 30 magnitudes of extinction at visible wavelengths. To look at the central regions of our galaxy, astronomers are forced to use wavelengths above $1\ \mu\text{m}$ (to infrared, micro, and radio waves). It is located at around 8 kpc (GRAVITY Collaboration et al., 2019) from the Sun, in the direction of the constellations Sagittarius, Ophiuchus and Scorpius.



Figure 1.1: The Milky Way's Galactic Center, the bright upper left part of the picture (Source: 2MASS/G. Kopan, R. Hurt - Atlas Image).

When we are talking about our Galaxy, we should describe the Galactic coordinate system.

1.2 Galactic coordinate system

Exploiting the natural symmetry introduced by the existence of the Galactic disk, IAU defined the Galactic coordinate system (see Blaauw et al., 1960). The orientation of **Galactic latitude** (b) and **Galactic longitude** (l) are defined from a vantage point taken to be the Sun (1.2). The Galactic midplane is not aligned with the celestial equator, but is inclined at an angle of 62.87° .

The J2000.0 equatorial coordinates of the north Galactic pole (NGP, $b = 90^\circ$) are:

$$\alpha_{\text{NGP}} = 12^{\text{h}}51^{\text{m}}26.28^{\text{s}} \quad (1.1)$$

$$\delta_{\text{NGP}} = 27^\circ 7' 41.7'' , \quad (1.2)$$

and the origin of the Galactic coordinate system ($l = 0^\circ$, $b = 0^\circ$) corresponds to:

$$\alpha_0 = 17^{\text{h}}45^{\text{m}}37.20^{\text{s}} \quad (1.3)$$

$$\delta_0 = -28^\circ 56' 9.6'' . \quad (1.4)$$

The location of the north celestial pole ($\delta_{\text{NCP}} = 90^\circ$) in Galactic coordinates correspond to:

$$l_{\text{NCP}} = 123^\circ 55' 55.2'' \quad (1.5)$$

$$b_{\text{NCP}} = 27^\circ 7' 41.7'' \quad (1.6)$$

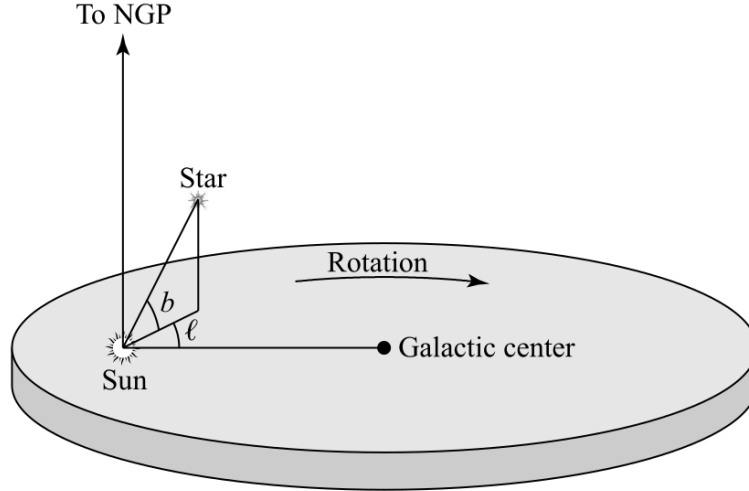


Figure 1.2: The definition of the Galactic coordinates l and b , with labeled direction of rotation (Source: Carroll and Ostlie (2017), p. 1045).

The transformation between equatorial and Galactic coordinates looks like this (assuming epoch J2000.0):

$$\begin{cases} \sin b & = \sin \delta_{\text{NGP}} \sin \delta + \cos \delta_{\text{NGP}} \cos \delta \cos(\alpha - \alpha_{\text{NGP}}) \\ \cos b \sin(l_{\text{NCP}} - l) & = \cos \delta \sin(\alpha - \alpha_{\text{NGP}}) \\ \cos b \cos(l_{\text{NCP}} - l) & = \cos \delta_{\text{NGP}} \sin \delta - \sin \delta_{\text{NGP}} \cos \delta \cos(\alpha - \alpha_{\text{NGP}}) . \end{cases} \quad (1.7)$$

Backwards transformation, from Galactic to equatorial coordinates looks like this (J2000.0 again):

$$\begin{cases} \sin \delta & = \sin \delta_{\text{NGP}} \sin b + \cos \delta_{\text{NGP}} \cos b \cos(l_{\text{NCP}} - l) \\ \cos \delta \sin(\alpha - \alpha_{\text{NGP}}) & = \cos b \sin(l_{\text{NCP}} - l) \\ \cos \delta \cos(\alpha - \alpha_{\text{NGP}}) & = \cos \delta_{\text{NGP}} \sin b - \sin \delta_{\text{NGP}} \cos b \cos(l_{\text{NCP}} - l) . \end{cases} \quad (1.8)$$

At present epoch, our solar system is only 30 pc above the Galactic midplane, which causes our line of sight to cross almost as much interstellar material as possible. However, based on the solar velocity (it is somewhat perpendicular to the Galactic plane), the Sun will reach an altitude of about 85 pc above the plane, which would place it in a very good observing location. Unfortunately, this will happen in only 15 million years (Carroll and Ostlie, 2017).

Even with the limited vision, we have been able to construct an image of the Galactic nucleus. First, we will take a look at its structure.

1.3 General structure

Looking at the Figure 1.3, we can see that the Galaxy has a **Halo** around it, that is around 50 kpc in diameter. Moving to the Galactic disk, we see the Galactic bulge in the middle of it. It is approximately 4-5 kpc in diameter, with $\sim 1.5 \times 10^{10} M_{\odot}$ of old stars with a complex and non-symmetric structure (see Portail et al., 2015). It consists of two different stellar populations. One of them are old stars, that compose the bulk of the mass. However, located in the innermost parts of the bulge, within the Central Molecular Zone (CMZ), resides the young population (Barbuy et al., 2018).

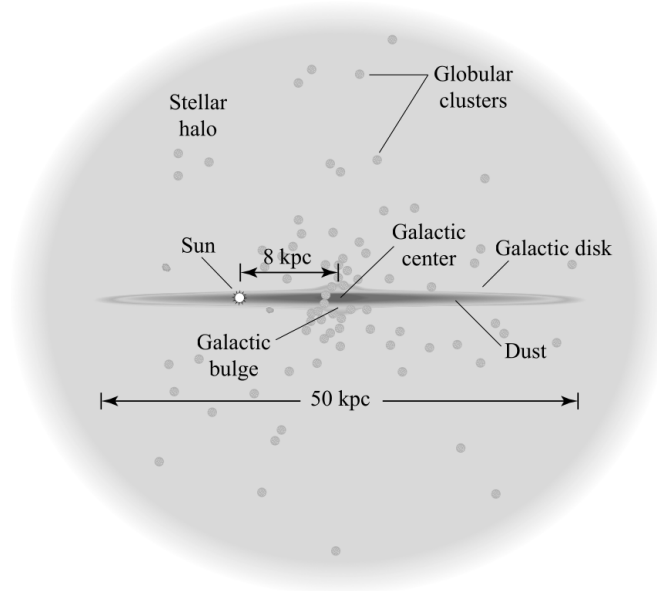


Figure 1.3: An edge-on diagram of the Galaxy, not to scale (Source: Carroll and Ostlie (2017), p. 1029).

1.4 Central Molecular Zone

CMZ is the largest reservoir of dense molecular gas in the Galaxy and is heavily obscured in the visible and near-IR wavelengths. It resides between $1.8^{\circ} > l > -1.3^{\circ}$ of Galactic longitude (Battersby et al., 2024), and is approximately 200 pc in radius. The total mass of

the gas is around $2 - 6 \times 10^7 M_{\odot}$. This corresponds to 3 – 10 % of the total molecular gas in the Galaxy, despite being only 0.1 % of projected surface (Henshaw et al., 2023). The CMZ includes all the largest Galactic Center’s cloud complexes, such as the 1.3° Cloud, Sgr B2, the 'Brick', Sagittarius A (Sgr A) clouds, and Sgr C (as shown in Figure 1.4).

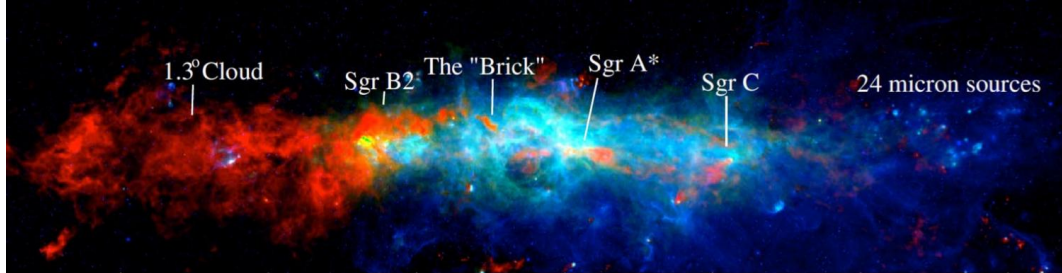


Figure 1.4: An infrared and multi-wave image of CMZ, with 24 μm sources highlighted (Source: C. Battersby).

Sgr A* is a supermassive black hole (SMBH), that resides in the center of the Milky Way. It is $\sim 4.1 \times 10^6 M_{\odot}$ (Ciurlo and Morris, 2025), and is surrounded by the Nuclear Star Cluster (NSC).

1.5 Nuclear Star Cluster

Nuclear Star Clusters are in the center of most galaxies. They are typically a few parsecs in size, have a mass of $10^5 - 10^7 M_{\odot}$ and luminosities of $10^6 - 10^7 L_{\odot}$ (Schödel et al., 2009). These star clusters are the densest known, and contain a mixed stellar population, with some signs of repeated episodes of star formation (Walcher et al., 2006). They are very compact and dense regions, which makes observations in external galaxies impossible, due to diffraction limit even for the 50 m-class telescopes (Schödel et al., 2009). Our own NSC, located only in 8 kpc, offers the best possibility to study them. Its size is estimated to be between 4.2 pc and 7.2 pc, with elliptical and flattened shape along Milky Way’s plane. The total luminosity is $\sim 4 \times 10^7 L_{\odot}$, and its mass falls between $2 \times 10^7 M_{\odot}$ and $4 \times 10^7 M_{\odot}$ (Neumayer et al., 2020). The majority of stars are old and evolved giants and supergiants (types K and M, with ages more than 5 billion years). However, there is a young population with more than 100 massive stars (Wolf-Rayet, O- and B-stars), that reside in the central 0.5 pc (Feldmeier-Krause et al., 2015).

With young stars being in such close vicinity to the Sgr A*, their formation *in situ* (‘in

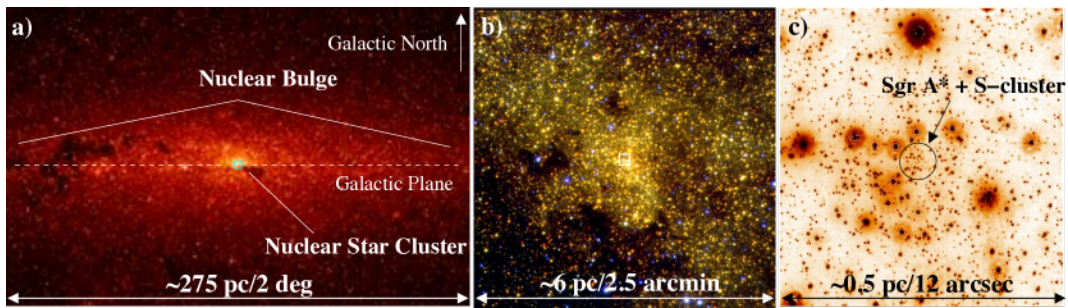


Figure 1.5: a) The Galactic Center. b) NSC. c) Sgr A* with S-cluster, central 0.5 pc of the Milky Way (Source: Schödel et al. (2014)).

its original place') is the most probable one. The age of those stars is very well constrained in 3 – 8 million years (Neumayer et al., 2020) range.

Gases, that are in vicinity of the Sgr A* (~ 0.1 pc), are believed to accrete into a disk (see Murchikova et al., 2019). This disk will be modeled and discussed later, in the Chapter 4.

Chapter 2

Supernovae and their explosions

The term **supernova** (SN) comes from Latin word *nova*, which means new. Prefix *super* distinguishes SNe from classical novae, because SNe are much more luminous. So luminous in fact, that their peaks are comparable to that of an entire galaxy. SNe explosions occur in the last stage of massive stars evolution. The physical nature of the process is either gravitational collapse of the stellar core, forming a neutron star or even a black hole, or completely disintegrating the original star (usually referred as progenitor).

2.1 Classification of supernovae

SNe are historically divided into two main branches - Type I and Type II. Their difference between them lies in the spectral features. Type I SNe do not have hydrogen lines near maximum light, whereas Type II SNe show strong ones. In a somewhat more detailed look, we can classify 5 different types based on spectra near maximum light (as shown in Figure 2.1).

2.1.1 Type I SNe

As shown in Figure 2.1, Type I SNe can be divided into subtypes Ia, Ib and Ic. Since hydrogen is the most abundant element in the Universe, the absence of hydrogen lines in their spectra suggests that the involved stars have been stripped off their hydrogen envelopes. Type Ia SNe could be found in any type of galaxy, whereas Types Ib and Ic have been seen only near regions of the recent star formations in spiral galaxies (Carroll and Ostlie, 2017, p. 585). Thus, short-lived massive stars are probably involved in Types Ib and Ic SNe, but not with

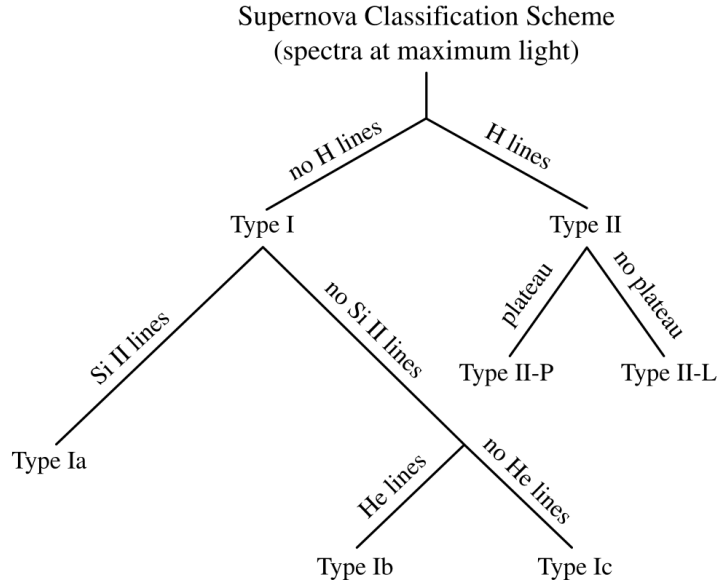


Figure 2.1: The classification of SNe based on their spectra near maximum light (Source: Carroll and Ostlie (2017), p. 587).

Type Ia. Type Ia SNe occur in thermonuclear explosions of CO white dwarfs, that are in the close binary star systems (Kurfürst, 2010). The mass transfer causes the white dwarf to reach the Chandrasekhar limit of $\sim 1.4 M_{\odot}$. Their light curves are extremely similar, which makes them being regarded as *standard candles*, used to determine distances in the Universe. The radioactive decay of $^{56}\text{Ni} \rightarrow ^{56}\text{Co}$, and later to the stable ^{56}Fe , radiates an enormous amount of gamma rays for over 100 days. The reprocessing of those gamma rays to the visible wavelengths is the main source of luminosity of these SNe, at least in the early phase, up to about 150 days (Kurfürst, 2010).

Types Ib and Ic lack the Si II lines near 615 nm (Type Ia SN has them), and the difference between each other lies in presence (Ib) or absence (Ic) of strong helium lines. Their origins are similar to Type II's (core collapse), with these events being fundamentally different from Type Ia SNe (Carroll and Ostlie, 2017, p. 586).

2.1.2 Type II SNe

When talking about Type II SNe (as well as Types Ib and Ic), we are talking about **core-collapse SNe**. A typical Type II releases $\sim 10^{46}$ J of total energy, with about 1 % being the kinetic energy of the ejecta, 0.1 % being photons, while the biggest fraction is radiated as neutrinos.

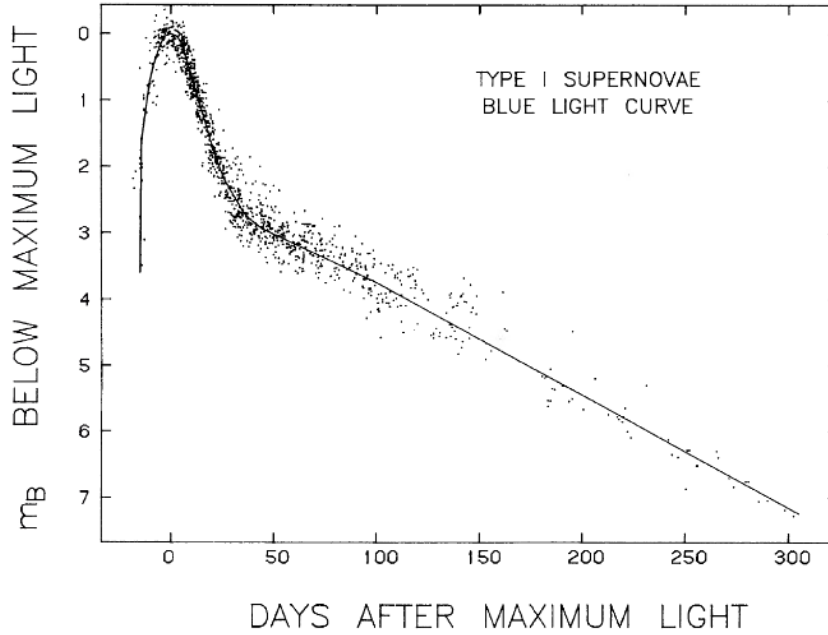


Figure 2.2: Composite light curve for Type I SNe, with all magnitudes being relative to the blue maximum m_B .

Core-Collapse Mechanism

Through its evolution, a massive star synthesizes different elements. For a $20 M_\odot$ star, the core hydrogen burning (the main-sequence lifetime) lasts for $\sim 10^7$ years, with next phase being the core helium burning ($\sim 10^6$ years). After He exhaustion begins the carbon burning, which lasts only about 300 years. Oxygen burning takes ~ 200 days, and the silicon is completed in only two days. At this point, temperatures in the core are extremely high, with photons having enough energy to destroy heavy nuclei (by **photodisintegration**). With extreme conditions ($T_c \sim 10^{10}$ K, $\rho_c \sim 10^{13}$ kg m $^{-3}$) free electrons that were supporting the star by degeneracy pressure, are captured by protons and heavy nuclei from the photodisintegration (inverse β -decay):



The amount of energy that escapes through neutrinos is enormous, having much higher power than the photon luminosity (Carroll and Ostlie, 2017, p. 590). With electron degeneracy gone, there is not enough pressure to support the core, and it begins to rapidly collapse. The outer layers of the star may still remain at the same place but the core collapse

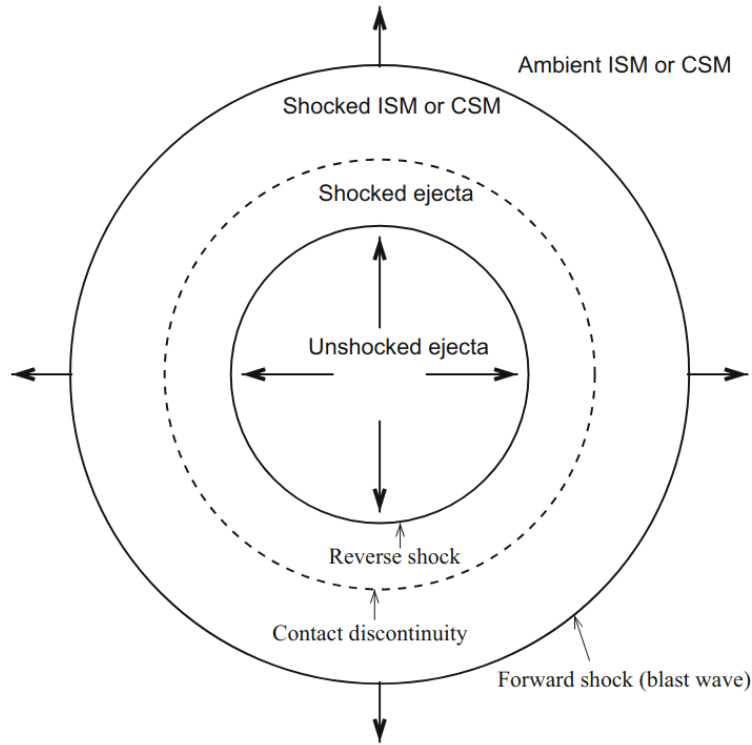


Figure 2.3: Scheme of the SN explosion. (Source: Smith et al. (2008))

continues until the density becomes higher than that of an atomic nucleus. At this point, the strong force suddenly becomes repulsive (due to neutron degeneracy), and the rebound of the inner core sends pressure waves outwards. After reaching the sound speed, the resulting shock wave heats and accelerates the material, which expands and radiates. During the expansion, the internal energy in the expanding envelope changes to kinetic energy (Kurfürst, 2010, p. 36). The shock reaches the surface of the star, releasing the envelope and the rest of the nuclear-processed matter outwards. As said before, total kinetic energy is in the order of $\sim 10^{44}$ J, being only $\sim 1\%$ of the total neutrino energy. When the material expanded enough (around 10^{13} m ≈ 100 AU), it becomes optically thin, and shows enormous peak luminosity of nearly 10^{36} W, or around billion solar luminosities. This brightness is competing with an entire galaxy, but for a very short time. Subsequent brightness changes determine their subclassification. Type II-P SNe show a distinct plateau in their light curves. It can extend to around 100 days, and is caused by progenitors, who are RSGs with significant hydrogen envelopes. The balance between cooling and recombination in the ejecta creates this plateau phase (Gall et al., 2015).

The process described above is believed to be the general mechanism of Types II, Ib and

Ic SNe. The difference between them lies in composition and mass of the envelope. Type II SNe are more common than Types Ib and Ic, and they are usually red supergiants (RSG), being at the time of core-collapse in the upper-right corner of H-R diagram. Types Ib and Ic, meanwhile, have lost various fractions of their envelopes before the explosion. They may correspond to the explosion of WN and WC Wolf-Rayet stars, respectively.

2.2 Explosions and interactions

For better description and analysis, we can look at a simpler analogous problem, which is the Riemann-Sod shock tube. It is essential in understanding the physics of the explosion shock front. To be accurate, we also have to acknowledge the Sedov blast-wave problem, which is a very good analogy for the explosion profiles (more about Sedov problem in Chapter 4).

2.2.1 Riemann-Sod shock tube

The Riemann-Sod shock tube, often simply called the Sod shock tube, is a specific type of the Riemann problem. Riemann problem involves a conservation law (like those in the Euler equations) along with piecewise constant initial data that has a single discontinuity. We can describe it as a long, straight tube filled with an ideal gas. At the initial time ($t = 0$), a thin diaphragm instantaneously separates the tube into two sections with different pressures and densities, while the gas is initially at rest in both sections (Sod, 1978):

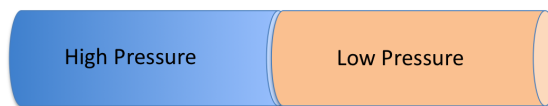


Figure 2.4: Initial conditions of the Sod shock tube problem. The right part of the tube has higher pressure and density. (Source: VH-1)

After the diaphragm is instantaneously removed, a complex wave pattern is emerged. In general, there is a backward shock (or rarefaction wave), which is moving backwards (to the left on the Figure 2.4), the initial contact discontinuity (CD) which moves forwards, and the forward shock which is also moving forwards, although faster than the CD. The profiles in some small time after the diaphragm removal look like this:

As shown in Figure 2.5, the CD is located around 0.7 on x/y/z axis. It is very distinct in density and internal energy (same 'trend' as temperature) profiles. Meanwhile, pressure

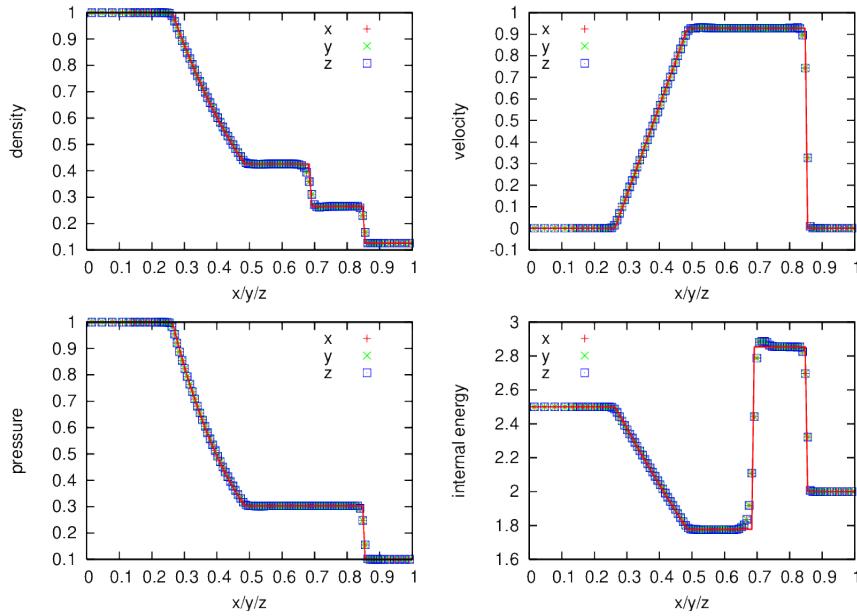


Figure 2.5: Profiles of density (top-left), velocity (top-right), pressure (bottom-left) and internal energy (bottom-right). (Source: Castro code, default Sod shock tube problem)

and velocity don't really show CD in their profiles. The forward shock wave is very well seen in every variable (around 0.85 on horizontal axis).

Overall, we can highlight some features from every profile. Density has two distinct 'steps', with first being the CD, and second being the forward shock. Temperature (internal energy) also has a big change at CD, spiking to a somewhat constant high value, with a steep drop to the initial condition of the right side at forward shock. Pressure and velocity profiles don't show the CD, but both have 'steps' at the forward shock. The rarefaction wave is seen in every profile. The CD and the forward shock wave are present in the future discussion of SN explosion models.

Overall, this problem is very useful and relevant in analysis of some Riemann problems and shock wave propagation. The solution contains two different types of discontinuities (CD and shock) and a smooth rarefaction wave, which makes it an extremely useful test for any hydrodynamics numerical scheme or code.

Using this problem, we can better analyze the front of the SN explosion in Chapter 4.

Chapter 3

Astrophysical programs and codes

3.1 SNEC

The SuperNova Explosion Code is an open-source Lagrangian code made by Morozova et al. (2015). It is used to model a supernova explosion, given the model of the progenitor star and an explosion energy. SNEC solves the equations of Lagrangian hydrodynamics in spherical symmetry, supplement with radiative diffusion. Using the mass coordinate system, instead of spatial one, SNEC has a much more precise calculations in the supernova core, where a lot of the mass is located. Using progenitor model from MESA (Modules of Experiments in Stellar Astrophysics, Paxton et al. (2011)), SNEC produces a one dimensional model, which can be later passed to a more advanced multidimensional code.

3.1.1 Equations

SNEC uses three conservation equations. The mass conservation:

$$\frac{\partial r}{\partial m} = \frac{1}{4\pi r^2 \rho}, \quad (3.1)$$

the energy conservation equation:

$$\frac{\partial \epsilon}{\partial t} = \frac{P}{\rho} \frac{\partial \ln \rho}{\partial t} - 4\pi r^2 Q \frac{\partial v}{\partial m} - \frac{\partial L}{\partial m} + \epsilon_{\text{Ni}}, \quad (3.2)$$

and the momentum conservation equation:

$$\frac{\partial v}{\partial t} = -\frac{Gm}{r^2} - 4\pi r^2 \frac{\partial P}{\partial m} - 4\pi \frac{\partial(r^2 Q)}{\partial m}. \quad (3.3)$$

Here r is the radius, t is the time, ρ is the mass density, ϵ is the specific internal energy (energy per unit mass), P is the pressure, $v = \partial r / \partial t$ is the velocity of the matter, Q is artificial viscosity, and G is the gravitational constant. Mass coordinate is defined as:

$$\int_0^r 4\pi r'^2 \rho(r') dr', \quad (3.4)$$

the radiative luminosity L is:

$$L = -(4\pi r^2)^2 \frac{\lambda_{ac} \partial T^4}{3\kappa \partial m}. \quad (3.5)$$

The inclusion of the radiation diffusion term ($\partial L / \partial m$ in (3.2)) is optional, that means that SNEC can be run either in pure hydro or in radiation-hydro mode.

ϵ_{Ni} from (3.2) is the specific energy deposited due to the radioactive decay of ^{56}Ni , which is local heating rate in each grid point $\epsilon_{\text{rad}} d$. Here, ϵ_{rad} is the time dependent rate of energy release per gram of radioactive nickel:

$$\epsilon_{\text{rad}} = 3.9 \times 10^{10} e^{-t/\tau_{\text{Ni}}} + 6.78 \times 10^9 (e^{-t/\tau_{\text{Co}}} - e^{-t/\tau_{\text{Ni}}}) \text{ erg g}^{-1} \text{ s}^{-1}, \quad (3.6)$$

and d is the deposition function:

$$d = \frac{1}{4\pi} \oint \frac{4\pi\kappa_\gamma}{\epsilon_{\text{rad}}} I d\omega. \quad (3.7)$$

In (3.6) $\tau_{\text{Ni}} = 8.8 \text{ d}$ and $\tau_{\text{Co}} = 113.6 \text{ d}$ are the mean lifetimes of ^{56}Ni and ^{56}Co respectively. Deposition function used solid angle ω , energy-integrated intensity I and effective gamma-ray opacity κ_γ , which is assumed to be purely absorptive and independent of energy. It is equal to $\kappa_\gamma = 0.06 Y_e \text{ cm}^2 \text{ g}^{-1}$, where Y_e is the electron fraction (Morozova et al. (2015)).

3.1.2 Equations of state and numerical scheme

SNEC provides 2 different equations of state (EOS), first of which is the ideal single-particle Boltzmann Gas EOS:

$$P = k_B N_A \rho T, \quad \epsilon = \frac{k_B N_A T}{\Gamma - 1}, \quad c_s^2 = \Gamma k_B N_A T, \quad (3.8)$$

where k_B is Boltzmann's constant, N_A is Avogadro's constant and $\Gamma \equiv c_p/c_V$ is the ratio of specific heats, chosen to be 1.4 here. This EOS is not recommended for the calculations, and its main purpose in SNEC is to pass the Sedov blastwave test. Usually code is used with the Paczynski EOS, which is a simplified analytic EOS for a mixture of ions, photons, and semi-degenerate/semi-relativistic electrons (see Paczynski, 1983). It is a bit modified, with the addition of corrections due to the partial ionization (see Morozova et al., 2015). In general, the total pressure is calculated as a sum of contributions from the ions, electrons and radiation:

$$P = P_{\text{ion}} + P_e + P_{\text{rad}} \quad (3.9)$$

SNEC's hydrodynamics scheme is based on Mezzacappa and Bruenn (1993). However, the code uses the simpler original von Neumann & Richtmyer form of artificial viscosity (see Von Neumann and Richtmyer, 1950). The timestep used in the update of the hydrodynamic equations must not be larger than the time it takes a sound wave to travel across a grid cell. Courant-Friedrichs-Lewy factor (CFL) is set to be 0.95 for stability.

3.2 Castro

Castro is an adaptive mesh, radiation/MHD hydrodynamics code that is designed to model astrophysical reacting flows on parallel computers (Almgren et al., 2020). Additionally, Castro has self-gravity (Katz et al., 2016), nuclear reaction and radiation physics (Zhang et al. (2011) and Zhang et al. (2013)). This code can handle multi-dimensional problems in Cartesian, cylindrical or spherical coordinate systems. We can use the one dimensional models from SNEC, and evolve them in time in 2 dimensions.

3.2.1 Adaptive mesh refinement

A numerical technique known as adaptive mesh refinement (or AMR) involves adjusting the precision of the solution both dynamically and throughout the computation. Since areas featuring sharp changes, abrupt transitions, or discontinuities are particularly challenging to estimate accurately, the level of precision is region-dependent. AMR strategically positions more refined grids within these areas, enabling calculations with reduced spatial and temporal increments (Berger and Olinger, 1984). This approach boasts broad applicability, making no presumptions regarding the quantity or nature of regions, nor their movement direction. Furthermore, it doesn't require prior understanding of how the solution will develop, as the refinement occurs after each iteration. Castro employs AMR as a layered arrangement of logically-rectangular grids with concurrent refinement in both spatial dimensions and time, leveraging the AMReX library (Zhang et al., 2019). The integration method across this grid structure is a repeating process where all grids progress in time. Finer grids advance through several steps to align with the temporal progress of coarser grids, and subsequently, data across different levels are synchronized. Castro ascertains which zones should be marked for refinement in the subsequent regridding phase by employing integrated procedures that assess if the magnitudes themselves or their rates of change exceed a predefined limit.

3.2.2 Hydrodynamics

Castro uses the fully compressible equations for the conserved state vector

$$\mathbf{U} = (\rho, \rho\mathbf{u}, \rho E, \rho A_k, \rho X_k, \rho Y_k):$$

$$\frac{\partial \rho}{\partial t} = -\nabla \cdot (\rho\mathbf{u}) + S_{\text{ext},\rho}, \quad (3.10)$$

$$\frac{\partial(\rho\mathbf{u})}{\partial t} = -\nabla \cdot (\rho\mathbf{u}\mathbf{u}) - \nabla p + \rho\mathbf{g} + \mathbf{S}_{\text{ext},\rho\mathbf{u}}, \quad (3.11)$$

$$\frac{\partial \rho E}{\partial t} = -\nabla \cdot (\rho\mathbf{u}E + p\mathbf{u}) + \rho\mathbf{u} \cdot \mathbf{g} - \sum_k \rho q_k \dot{\omega}_k + \nabla \cdot k_{\text{th}} \nabla T + S_{\text{ext},\rho E}, \quad (3.12)$$

$$\frac{\partial \rho A_k}{\partial t} = -\nabla \cdot (\rho\mathbf{u}A_k) + S_{\text{ext},\rho A_k}, \quad (3.13)$$

$$\frac{\partial \rho X_k}{\partial t} = -\nabla \cdot (\rho\mathbf{u}X_k) + \rho \dot{\omega}_k + S_{\text{ext},\rho X_k}, \quad (3.14)$$

$$\frac{\partial \rho Y_k}{\partial t} = -\nabla \cdot (\rho\mathbf{u}Y_k) + S_{\text{ext},\rho Y_k}. \quad (3.15)$$

Here ρ is density, \mathbf{u} is velocity, T is temperature, p is pressure, \mathbf{g} is the gravitational vector, k_{th} is thermal conductivity, and $E = e + \mathbf{u} \cdot \mathbf{u}/2$ is the total energy, where e represents the internal energy, and $S_{\text{ext},\dots}$ are user-specified terms. X_k is the abundance of k^{th} isotope, with its production rate $\dot{\omega}_k$ and energy release q_k . Castro also carries around auxiliary variables Y_k and advected quantity A_k .

3.2.3 EOS

Castro can be supplied by user with any EOS. However, EOS must take (ρ, T, X_k) as input and return needed thermodynamic variables. Castro itself is supplied with a gamma-law, Helmholtz or Lattimer-Sweaty EOS (Zhang et al., 2013). Most of standard problems, including ones in this work, use the gamma-law:

$$p = \rho e(\gamma - 1) = \frac{\rho T k_{\text{B}}}{\mu m_p}, \quad (3.16)$$

where $\gamma = c_p/c_V$ is the ratio of specific heats, m_p is the mass of the proton, and μ is the mean molecular weight, which is equal to:

$$\frac{1}{\mu} = \sum_k \frac{X_k}{M_k}. \quad (3.17)$$

Here M_k is the atomic weight of the isotope k .

3.2.4 Radiation

If enabled, Castro can calculate hydrodynamics with radiation together, using Gray Radiation Hydrodynamics equations. The code adopts flux limiter λ with a simple rational approximations from Levermore and Pomraning (1981):

$$\lambda(R) = \frac{2 + R}{6 + 3R + R^2}, \quad (3.18)$$

$$R = \frac{|\nabla E_r^{(0)}|}{\chi_{\text{R}} E_r^{(0)}}, \quad (3.19)$$

where χ_R is the Rosseland mean of the sum of the absorption and scattering coefficients. And $E_r^{(0)}$ is equal to:

$$E_r^{(0)} = E_r + 2 \frac{\lambda}{\chi_R} \frac{\mathbf{u}}{c} \cdot \nabla E_r + O\left(\frac{v^2}{c^2}\right). \quad (3.20)$$

Following Krumholz et al. (2007) authors drop all insignificant terms in the following regimes: streaming, static diffusion, and dynamic diffusion limits. Keeping the terms up to $O(\frac{v}{c})$ radiation hydrodynamics equations become:

$$\frac{\partial \rho}{\partial t} + \nabla \cdot (\rho \mathbf{u}) = 0, \quad (3.21)$$

$$\frac{\partial(\rho \mathbf{u})}{\partial t} + \nabla \cdot (\rho \mathbf{u} \mathbf{u}) + \nabla p + \lambda \nabla E_r = 0, \quad (3.22)$$

$$\frac{\partial(\rho E)}{\partial t} + \nabla \cdot (\rho E \mathbf{u} + p \mathbf{u}) + \lambda \mathbf{u} \cdot \nabla E_r = -c \kappa_P (a T^4 - E_r^{(0)}), \quad (3.23)$$

$$\frac{\partial E}{\partial t} + \nabla \cdot \left(\frac{3-f}{2} E_r \mathbf{u} \right) - \lambda \mathbf{u} \cdot \nabla E_r = c \kappa_P (a T^4 - E_r^{(0)}) + \nabla \cdot \left(\frac{c \lambda}{\chi_R} \nabla E_r \right). \quad (3.24)$$

New quantities here are $a = \frac{4\sigma}{c}$, where σ is the Stefan-Boltzmann constant, κ_P is Planck mean interaction coefficients, and $f = \lambda + \lambda^2 R^2$ is the Eddington factor.

3.3 Sedona

Sedona is a code, that is primarily focused on calculating the radiation signatures of SNe and other transient phenomena. Its radiation transport calculation is done via an implicit Monte Carlo algorithm (Roth and Kasen, 2015). With multi-dimensional model from Castro, we can calculate light curves and spectra. Sedona generates the time series of synthetic light curves $L_{\{v\}}(\{t\})$ at frequencies $\{v\}$ and output times $\{t\}$. All given formulas can be found in the Sedona6 documentation. The bolometric luminosity is simply given as:

$$L_{\text{bol}}(\{t\}) = \int_{\{v\}} L_{\{v\}}(\{t\}) dv. \quad (3.25)$$

The absolute bolometric magnitude is given as:

$$M_{\text{bol}} = -2.5 \log_{10} L_{\text{bol}} + 88.697425. \quad (3.26)$$

In order to look at our light curves in certain filters, we have to convolve it with a given transmission curve. Let's say that $T_b(\nu)$ is the transmission for a given filter band b at frequency ν . In this case the convolved luminosity will look like this:

$$\mathcal{L}_\nu(b) = \frac{\int T_b(\nu)L_\nu d \ln \nu}{\int T_b(\nu) d \ln \nu} . \quad (3.27)$$

To convert this formula to an AB magnitude, we need to use this equation (Kurfürst, 2010, p. 75):

$$M_{\text{AB}}(b) = -2.5 \log_{10} \left(\frac{\mathcal{L}_\nu(b)}{4\pi d^2} \right) - 48.60 , \quad (3.28)$$

where $d = 10$ pc.

3.4 MetaCentrum

A lot of calculations in this work were done through MetaCentrum. It manages a distributed computing infrastructure consisting of computing and storage resources owned by CESNET as well as joint academic institutes in the Czech Republic. Their cloud-computing services were invaluable and interesting to work with. Whole process works through sftp connection. To interactively work with MetaCentrum's resources, request should be formed. It consists of number of machines, number of cores, amount of RAM memory and usage time. After waiting in queue (which depends on the request), one can work with given resources. Usually it consists of some bash script, that handles binaries and files. Interactive mode gives an opportunity to look at the calculations 'in real time', and easily check for errors and results during them. However, this mode also forces a user to keep their terminal (and thus machine and internet connection) running all time. To avoid this, you can send a specific bash file, with the request inside. This way you can forget about the queue and calculations, and just turn your machine off. However, to check the results you have to visit MetaCentrum's website and look at your running 'jobs'. Also you can set up email notifications in case some error occurs (which frequently happens). Overall, MetaCentrum is an amazing resource for any type of numerical tasks.

Chapter 4

Models

This work used different initial locations around the Galactic accretion disk to interact with identically parameterized SN explosion. The progenitor was a hydrogen-rich RSG, with a mass of $15 M_{\odot}$ and radius of $\sim 1050 R_{\odot}$. SN profiles immediately after the shock breakout, that were generated by the SNEC code, look like this:

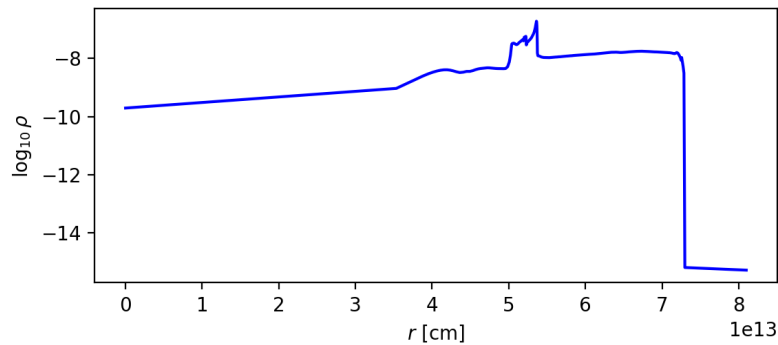


Figure 4.1: Profile of the logarithm of density, created by the SNEC code.

This generated profiles are used in every subsequent model. And for comparative reasons, let's first look at the isolated SN explosion without any surrounding material.

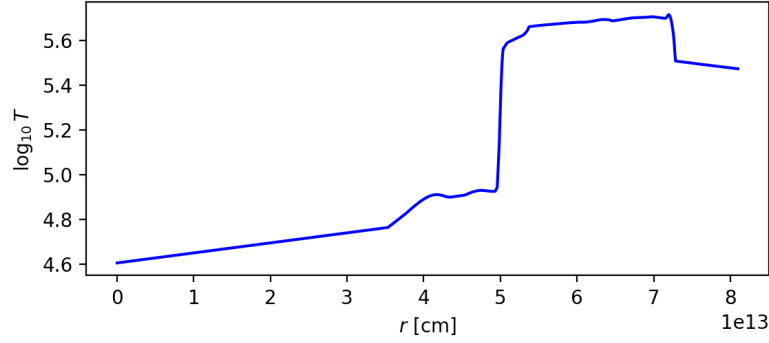


Figure 4.2: Profile of the logarithm of temperature, created by the SNEC code.

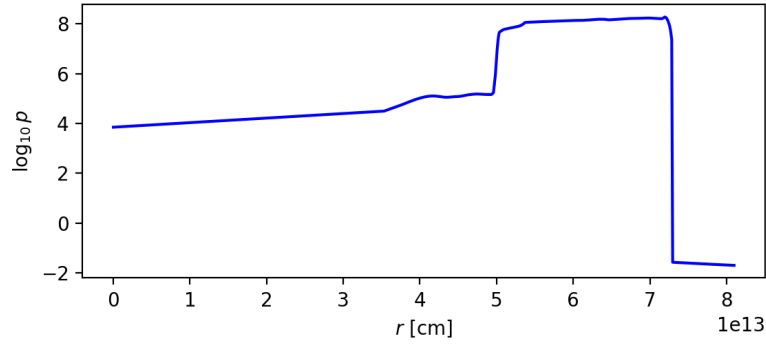


Figure 4.3: Profile of the logarithm of pressure, created by the SNEC code.

4.1 Isolated supernova

These calculations were done with Castro, in one-dimensional spherical coordinates. Without any material around, the SN ejecta expands freely. The profiles of density, temperature and velocity at 30 and 200 days are shown in Figures 4.4, 4.5 and 4.6.

The density profile has a distinct 'step' in front, after the first drop (which is the CD). It is a shock wave, discussed in the Riemann-Sod shock tube section. Velocity is very linear from the center to the CD, which looks exactly like Sedov blast wave velocity profile, as shown in Figure 4.7. This almost exactly resembles the so-called homologous expansion where the velocity is proportional to the distance, $v \sim r$.

Temperature drops right after CD, and creates a very thin (due to extreme radiation cooling) peak at the front shock. There are also some evident internal shocks in density and temperature profiles.

This simpler model was very useful for the understanding of the main models and

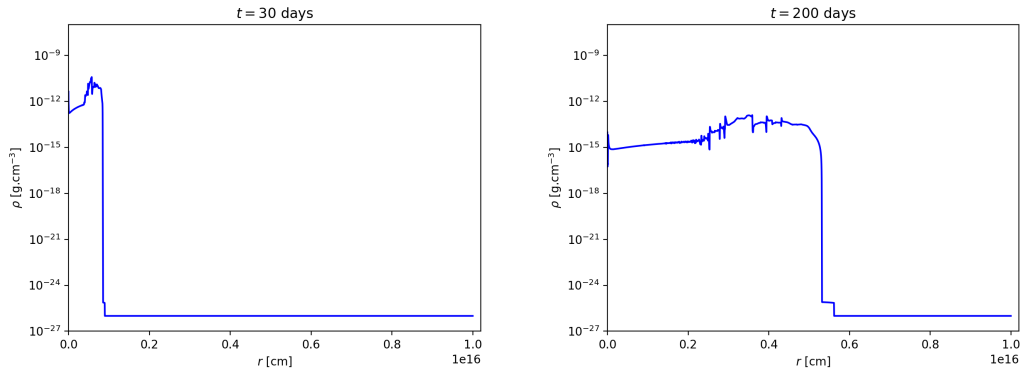


Figure 4.4: Density profiles with logarithmic scale at $t = 30$ days and $t = 200$ days.

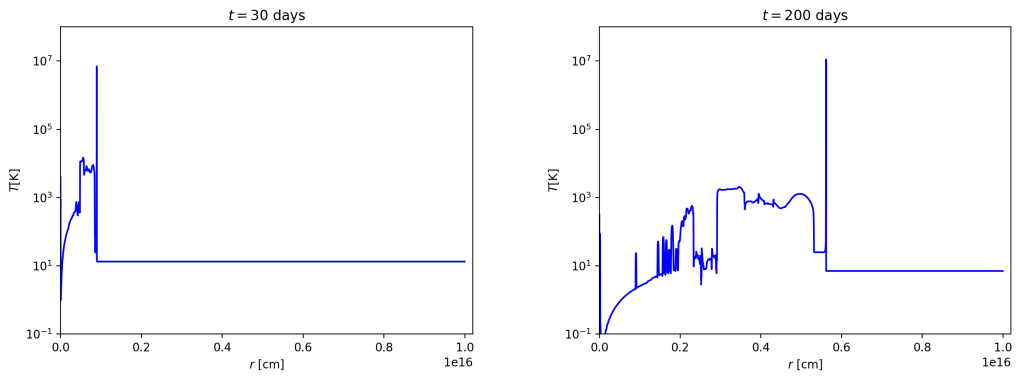


Figure 4.5: Temperature profiles with logarithmic scale at $t = 30$ days and $t = 200$ days.

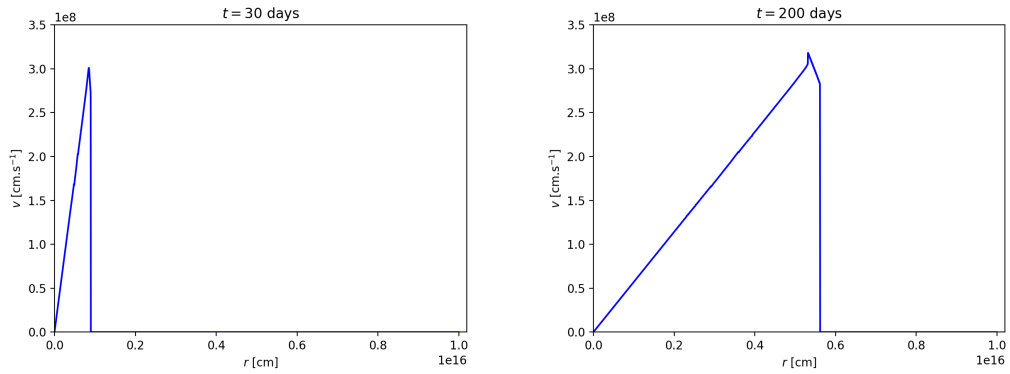


Figure 4.6: Velocity profiles with regular scale at $t = 30$ days and $t = 200$ days.

radiation-hydrodynamics Castro code. It exhibits some of the same features in its profiles, such as the forward shock wave, CD, and approximately linear velocity magnitude rise.

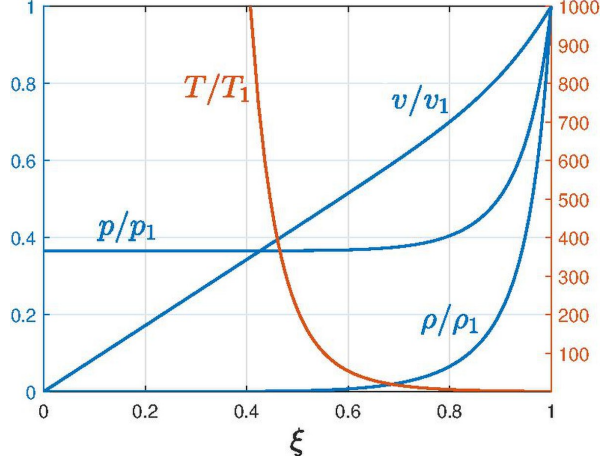


Figure 4.7: Profiles of velocity magnitude, density, temperature and pressure in Sedov blast wave problem, with a very linear velocity profile. (Source: Self-similar solution of Taylor-von Neumann-Sedov blast wave, Sunlitsky 2021)

4.2 SN surroundings, disk model

In our model, we used an accretion disk around a supermassive black hole, to interact with SN explosion. Mass of the SMBH is $M_{\text{SMBH}} = 4 \times 10^6 M_{\odot}$, and it is located outside the domain. The disk geometry is described by the parameters in the next section.

Two-dimensional disk model

Gravitational potential from the SMBH is:

$$\phi = -\frac{GM_{\bullet}}{r}, \quad (4.1)$$

where G is the gravitational constant, M_{\bullet} is SMBH mass and r is the spherical distance. If we rewrite it in cylindrical coordinates R and z (symmetrical in the azimuthal coordinate φ):

$$\phi = -\frac{GM_{\bullet}}{(R^2 + z^2)^{1/2}}. \quad (4.2)$$

From the potential, we can easily find radial and vertical gravitational acceleration components (by calculating $-\vec{\nabla}\phi$) in case of the approximation by a thin disk (Kurfürst, 2015)

$$g_R = -\frac{GM_{\bullet}R}{(R^2 + z^2)^{3/2}}, \quad g_z = -\frac{GM_{\bullet}z}{(R^2 + z^2)^{3/2}}. \quad (4.3)$$

Vertical hydrostatic equilibrium can be described by

$$\frac{dP}{dz} = \rho g_z, \quad (4.4)$$

with use of Eq. (4.3), it is

$$\frac{dP}{dz} = -\rho \frac{GM_* z}{(R^2 + z^2)^{3/2}}. \quad (4.5)$$

In an isothermal approximation (where $P = a^2 \rho$ and the sound speed a^2 is regarded as constant), the density ρ of such a disk takes the Gaussian profile Kurfürst (2015); it looks like this:

$$\rho = \rho_0 \cdot e^{-\frac{GM_* z^2}{a^2 R^3}}, \quad (4.6)$$

where ρ_0 is the disk midplane density,

$$\rho_0 = \Sigma_0 \left(\frac{r_g}{R}\right)^2 \sqrt{\frac{GM_*}{2\pi a^2 R^3}}, \quad (4.7)$$

where r_g is the gravitational radius of the black hole, $r_g = 2GM_*/c^2$. For our problem, initial vertically integrated (surface) density is $\Sigma_0 \approx 10^{11} \text{ kg m}^{-2}$ and $r_g \approx 10^7 \text{ km}$.

The Galactic disk accretion rate \dot{M}_{disk} can be roughly inferred from Eddington limit, thus,

$$\dot{M}_{\text{disk}} = \dot{M}_{\text{Edd}} = \frac{L_{\text{Edd}}}{\eta c^2}, \quad (4.8)$$

where η is the approximate accretion rate factor, chosen to be 0.1. The Eddington luminosity L_{Edd} , for a close to pure ionized hydrogen, can be found by (see Rybicki and Lightman, 1986)

$$L_{\text{Edd}} = \frac{4\pi GM_* m_p c}{\sigma_T}, \quad (4.9)$$

where m_p is the proton mass and σ_T is Thomson scattering cross-section for electrons. If we use our values, Eddington luminosity becomes

$$L_{\text{Edd}} \approx 5 \times 10^{37} \text{ W}, \quad (4.10)$$

from which the Galactic disk accretion rate is

$$\dot{M}_{\text{disk}} \approx 0.089 M_{\odot} \text{ yr}^{-1} . \quad (4.11)$$

Besides the disk, the region near the Galactic Center is filled with a very hot and very rare gas, whose temperature may be $\sim 10^7$ K (or even more) and its density is described by the Bondi accretion relations, see, e.g., Kurfürst et al. (2024). Under these conditions, the overall interstellar gas density in this region may be about $\sim 10^{-19} \text{ kg m}^{-3}$.

4.3 Calculated models

We calculated two characteristic models for two two fundamental SN-disk positions. One position is called the 'bottom' where the SN progenitor is located below the plane of the Galactic disk. The other position was selected to be inside the disk, at the disk midplane. In both models, the overall distance of the studied interaction region is about $\sim 10^4 r_g$. Due to the geometry of the problem, we were forced to work in Cartesian coordinate system, which brings some numerical problems, like the 'ornament' artifact (in the 'bottom' model).

Regarding the conditions in the surroundings reported in the previous Section, these models, however, show ambient temperature well below the listed one. The reason being the inclusion of radiation hydrodynamics which is necessary for subsequent radiation transfer calculations. The radiative cooling in the very rare ambient gas is so efficient that this would need much more sophisticated modeling to stabilize the ambient temperature at the desired level. However, this condition is easily achievable in case of the adiabatic solution (see Kurfürst et al., 2024) which is not the case of the proposed models due to absolute necessity of the radiation inclusion. Tyto modely ovšem ukazují teplotu okolního prostředí značně nižší než uvedených .

The 'bottom' model

One of the resulting models has the SN below the disk (or closer to the 'bottom' of the domain), ~ 300 AU from the midplane. The SMBH is located 2000 AU to the 'left' of the SN. The whole domain is 2000 AU \times 2000 AU in size. Resulting plots for density (Figure 4.8), temperature (Figure 4.9) and magnitude of the velocity (Figure 4.10) from the start of the

simulation (8 days) to 300 days are shown below.

For a greater diversity of the studied process, we included two different types of the close SN surroundings; in the 'bottom' we did not input the progenitor's stellar wind which we assume could be removed in this case by an arbitrary process in the Galactic Center region. On the other hand, in the following 'center' model such a stellar wind is initially included.

The 'center' model

The second model has the SN inside the Galactic disk (hence the 'center' model), shifted about 300 AU towards according to the first model. This time the stellar wind was also taken in consideration, resulting in a significant initial density profile around the disk unseen in the previous 'bottom' model. Resulting plots of density (Figure 4.11), temperature (Figure 4.12), and magnitude of the velocity (Figure 4.13) from the starting time of simulation (8 days) to 160 days are shown below.

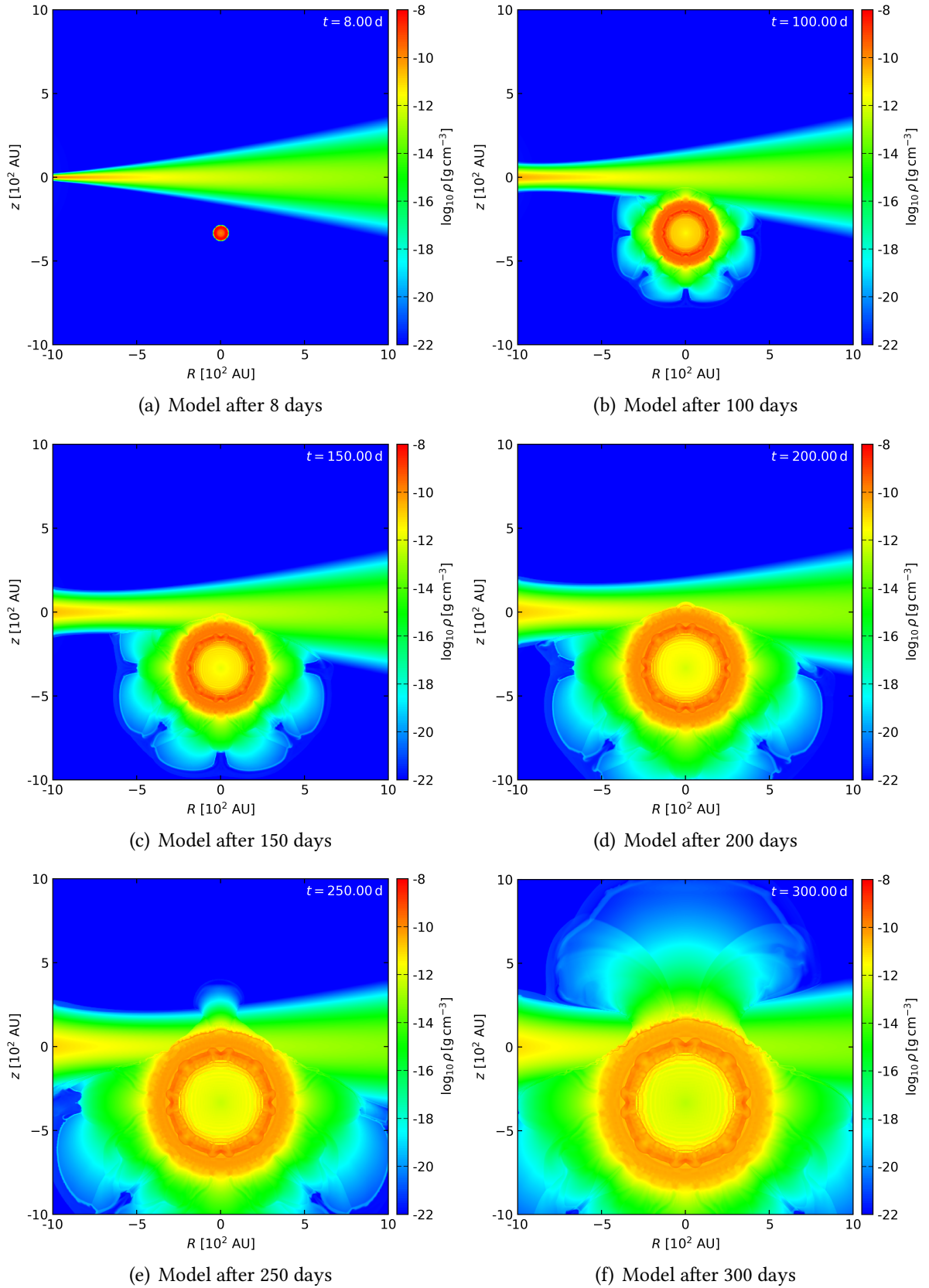
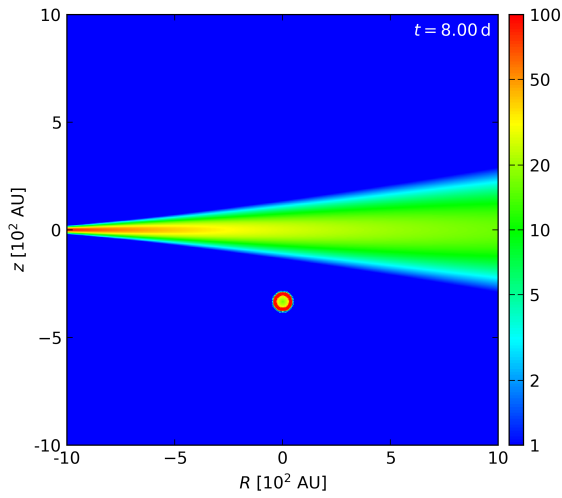
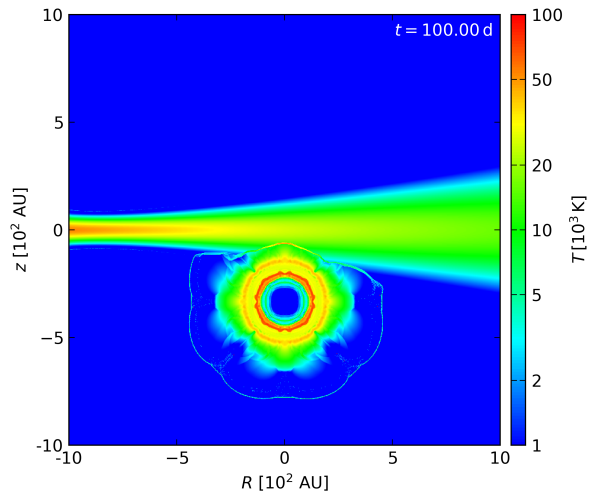


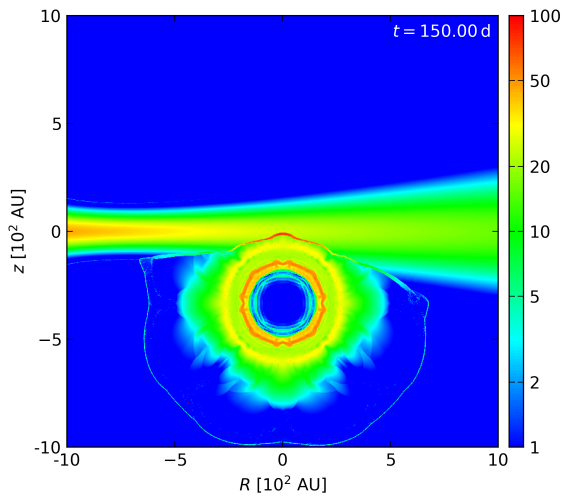
Figure 4.8: Pseudocolor plot of the logarithm of density after a) 8 days, b) 100 days, c) 150 days, d) 200 days, e) 250 days and f) 300 days.



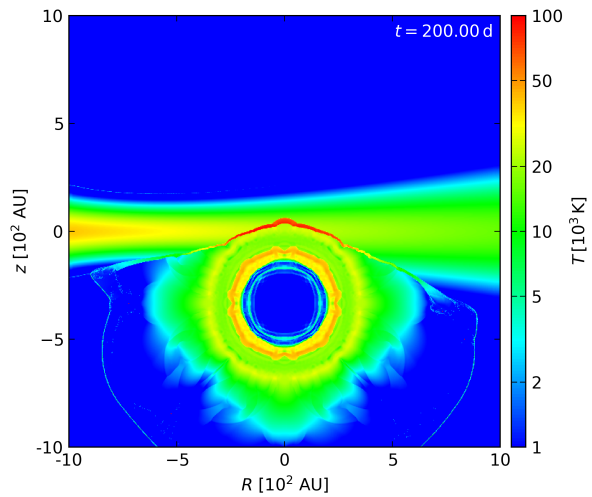
(a) Model after 8 days



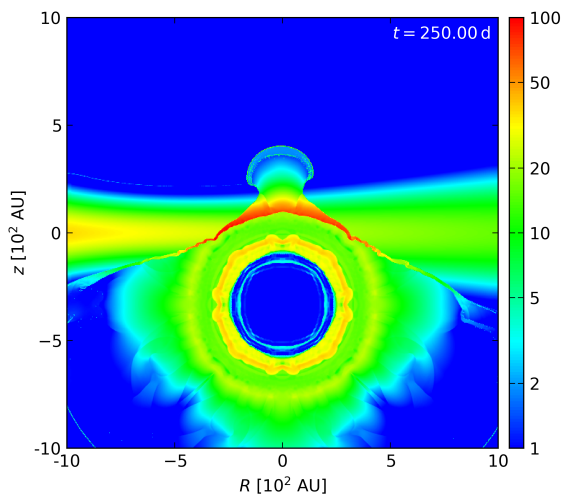
(b) Model after 100 days



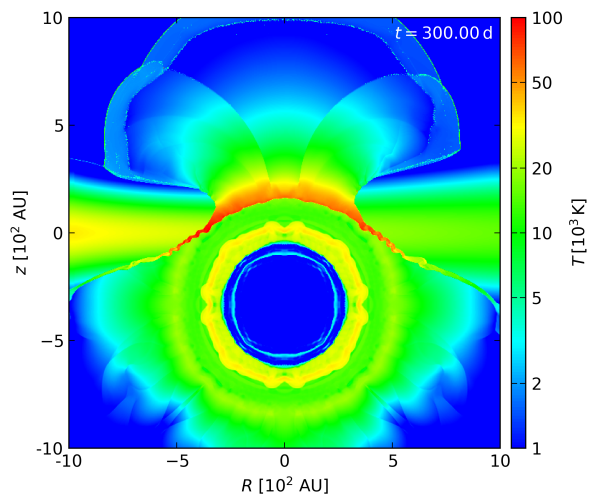
(c) Model after 150 days



(d) Model after 200 days



(e) Model after 250 days



(f) Model after 300 days

Figure 4.9: Pseudocolor plot of the logarithm of temperature after a) 8 days, b) 100 days, c) 150 days, d) 200 days, e) 250 days and f) 300 days.

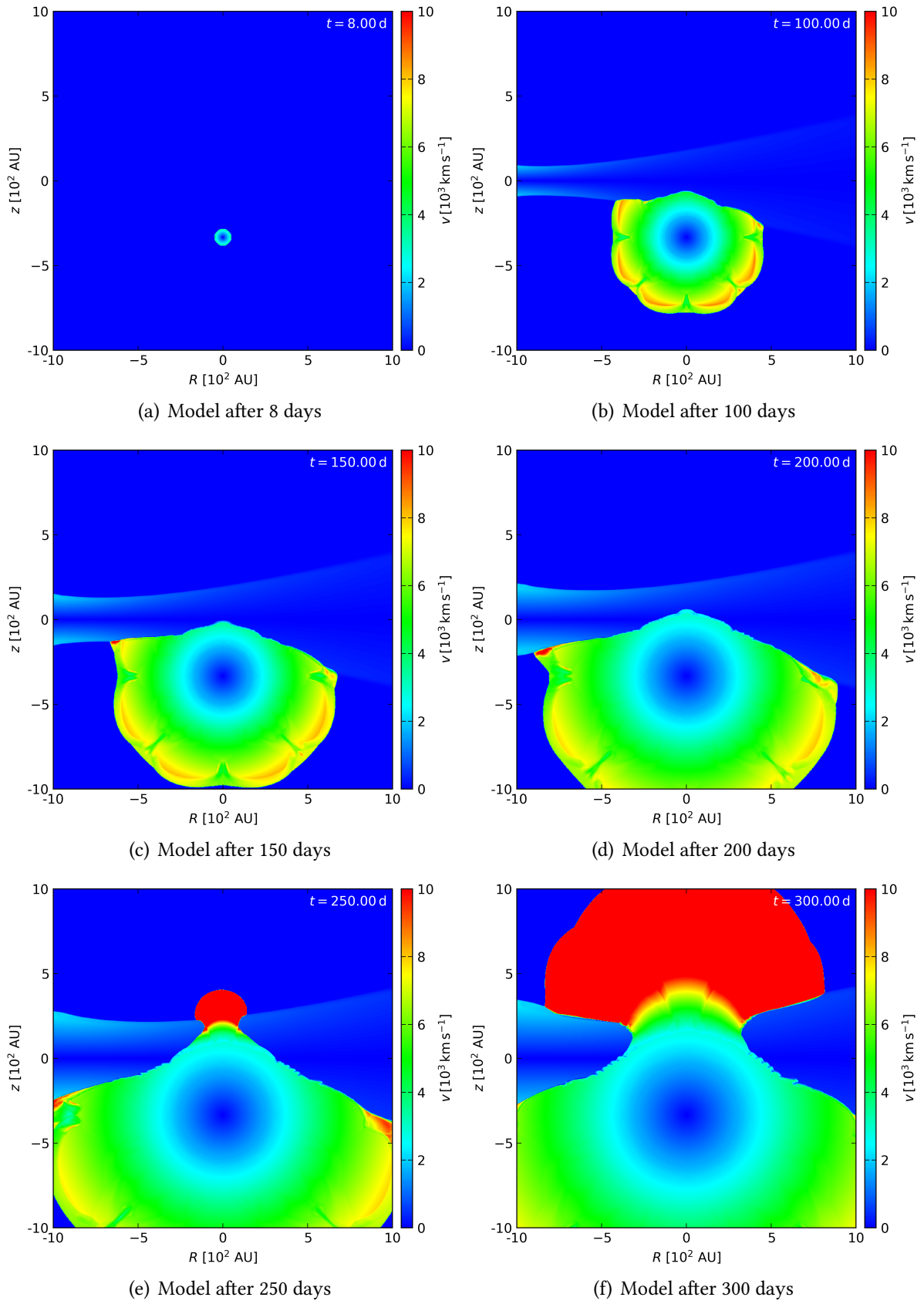


Figure 4.10: Pseudocolor plot of the absolute magnitude of velocity after a) 8 days, b) 100 days, c) 150 days, d) 200 days, e) 250 days and f) 300 days.

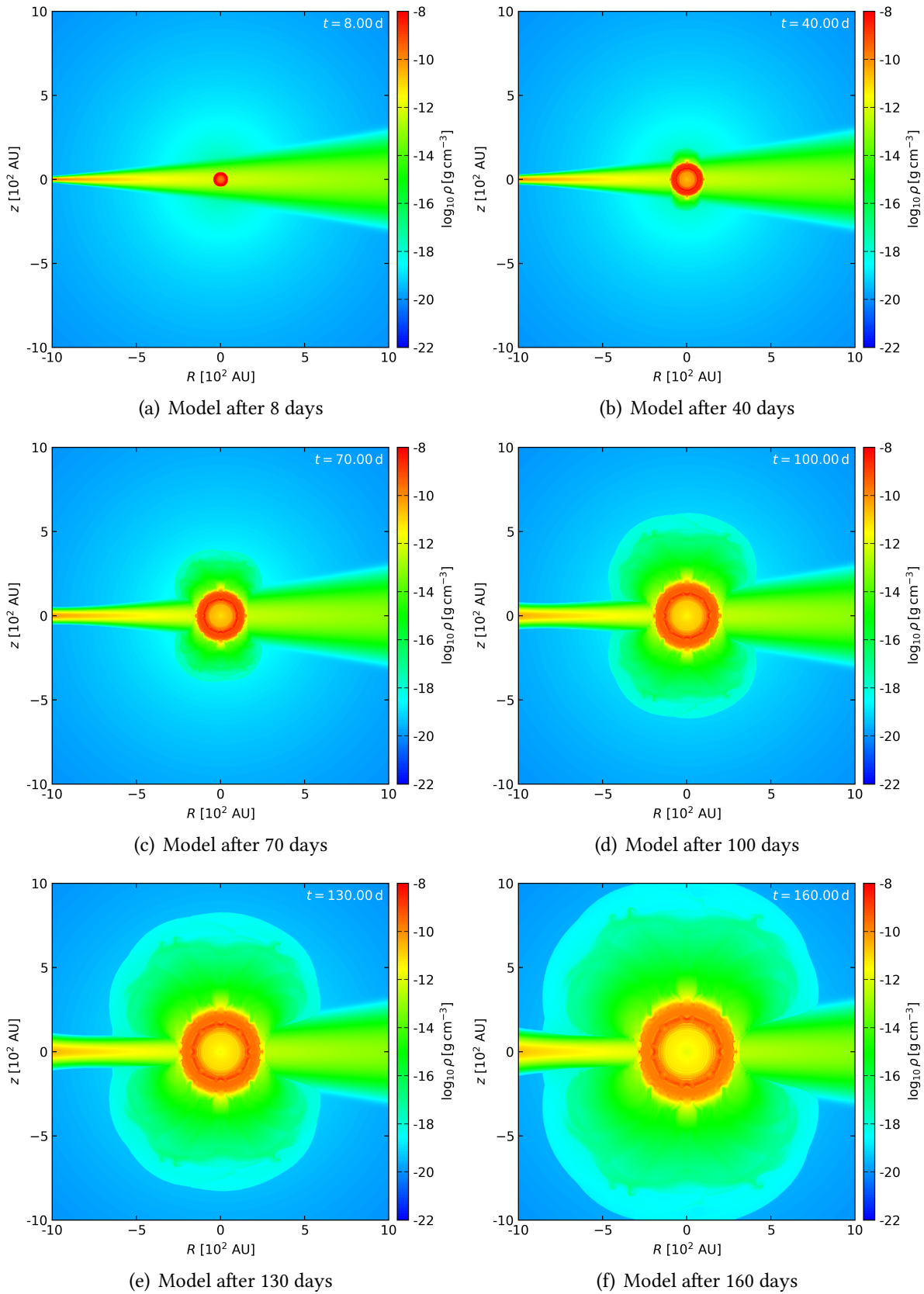


Figure 4.11: Pseudocolor plot of the logarithm of density after a) 8 days, b) 40 days, c) 70 days, d) 100 days, e) 130 days and f) 160 days.

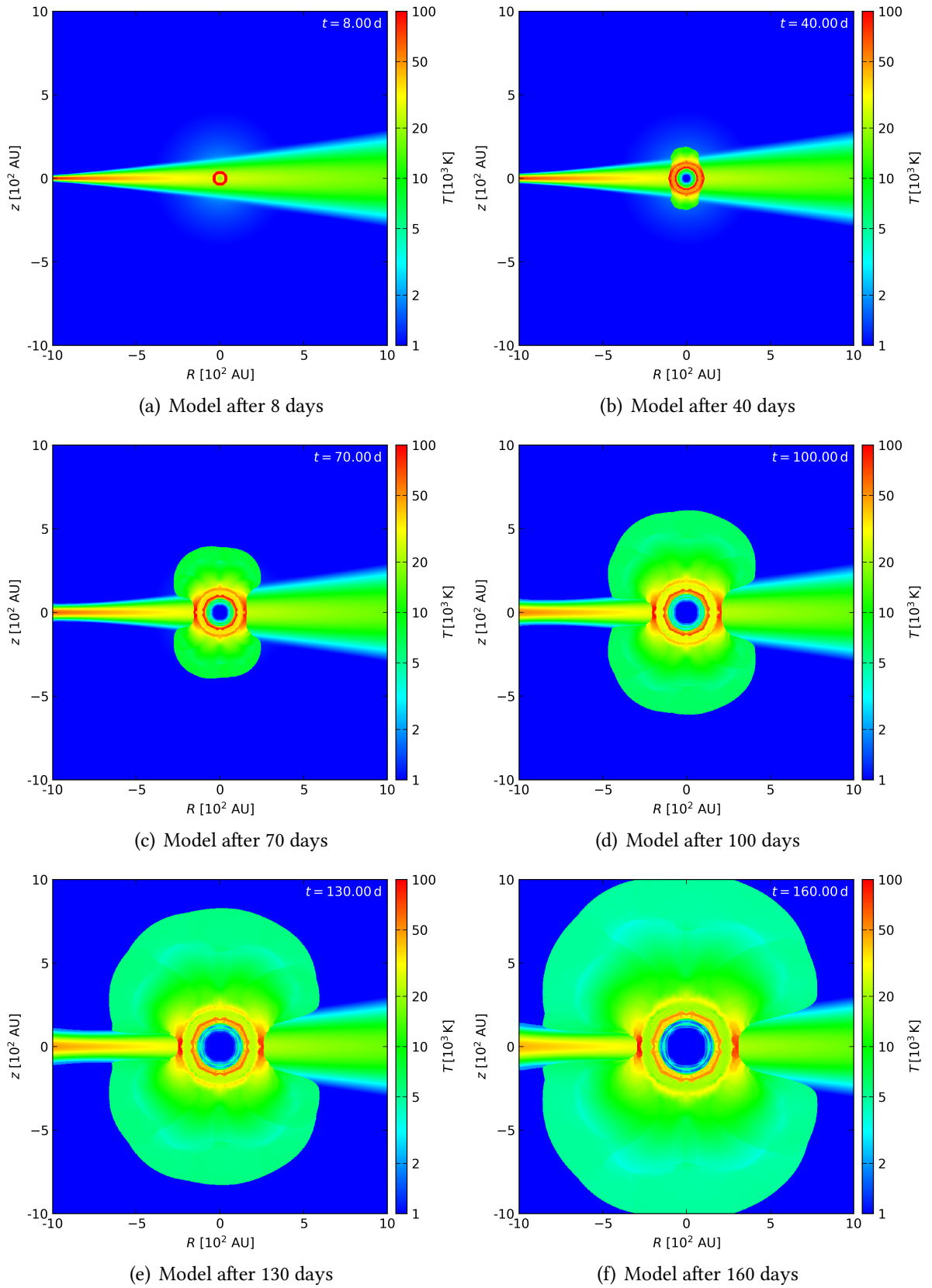


Figure 4.12: Pseudocolor plot of the logarithm of temperature after a) 8 days, b) 40 days, c) 70 days, d) 100 days, e) 130 days and f) 160 days.

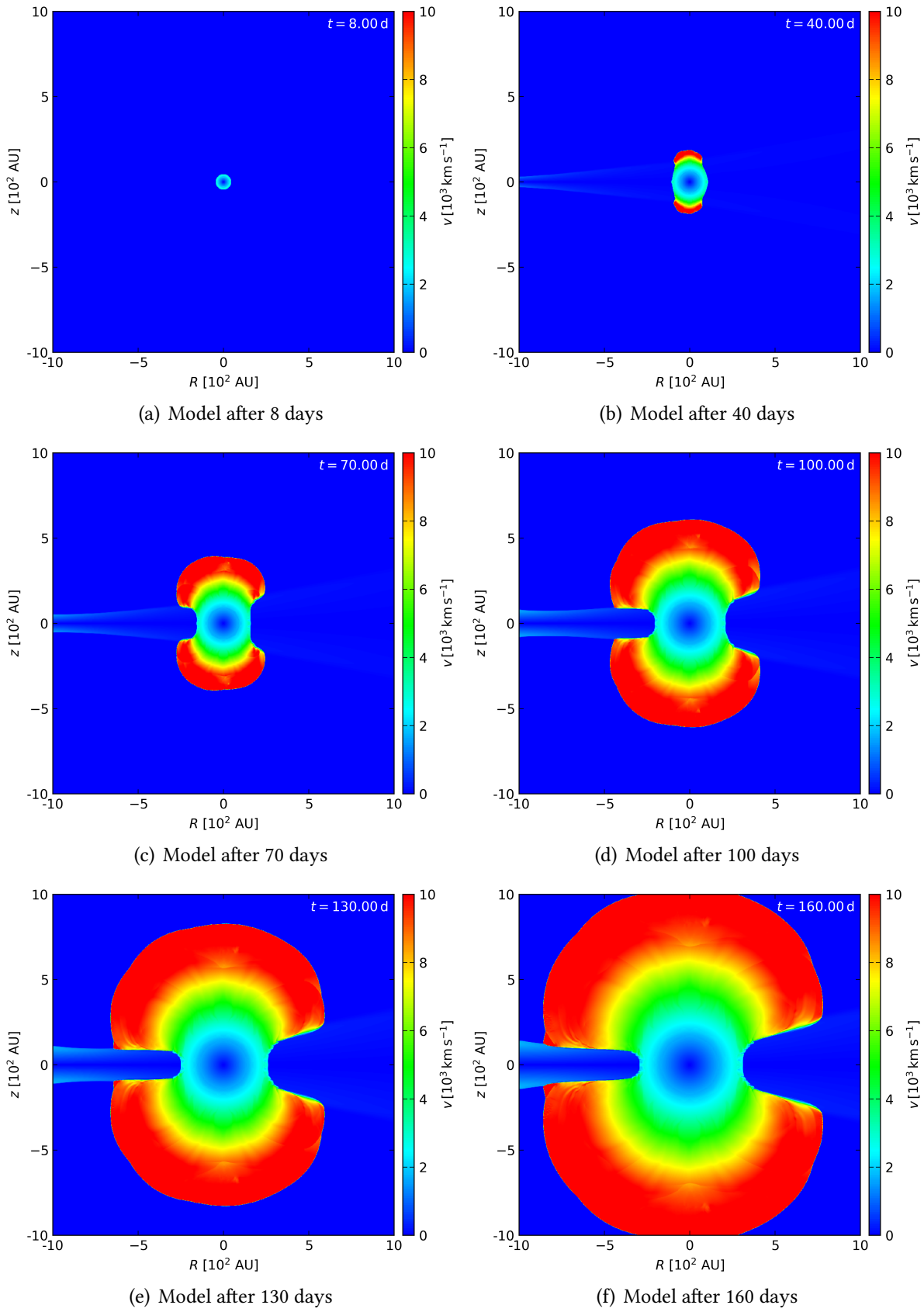


Figure 4.13: Pseudocolor plot of the absolute magnitude of the velocity after a) 8 days, b) 40 days, c) 70 days, d) 100 days, e) 130 days and f) 160 days.

4.4 Calculated light curves

Two light curves were generated from the 'bottom' model, with the top and bottom views on the domain:

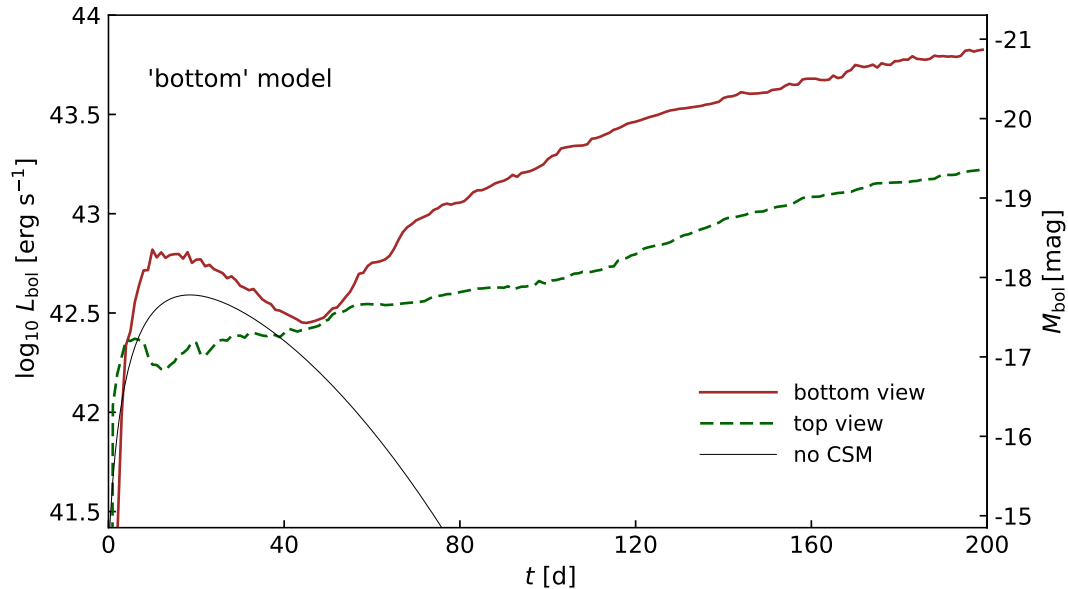


Figure 4.14: Logarithm of the bolometric luminosity and absolute bolometric magnitude of the 'bottom' model over 200 days. Solid black line shows an isolated SN explosion, with no circumstellar material (no CSM), calculated semianalytically using the Arnett's law, which were adapted from older models of Kurfürst et al. (2020).

Similar process was done for the 'center' model, but the views were chosen to be from top and left (instead of top and bottom). Figure 4.14 shows the results of the light-curve calculation for the 'bottom' model; the bottom view (the red line) shows after the sudden increase at the beginning the partial decrease in luminosity, which corresponds to the early phase expansion of SN into the 'empty' surroundings. After ~ 50 days, the luminosity begins to grow as the SN penetrates the much denser structure of the Galactic disk. The top-view profile (the green dashed line) does not exhibit the initial decrease, because the SN radiation is mostly reprocessed by the denser gas of the disk, which leads to a significantly smoother profile of the time evolution of the luminosity.

This is not the case of the 'center' mode where the initial SN explosion is more obscured by the disk, so the luminosity evolution is in this case roughly monotonic. However, we demonstrate in the 'center' model the light curves seen from the bottom and from the right (equatorial view); the latter shows significantly higher statistical noise caused by the lack of photon packets that were able to pass through the longitudinal size of the disk.

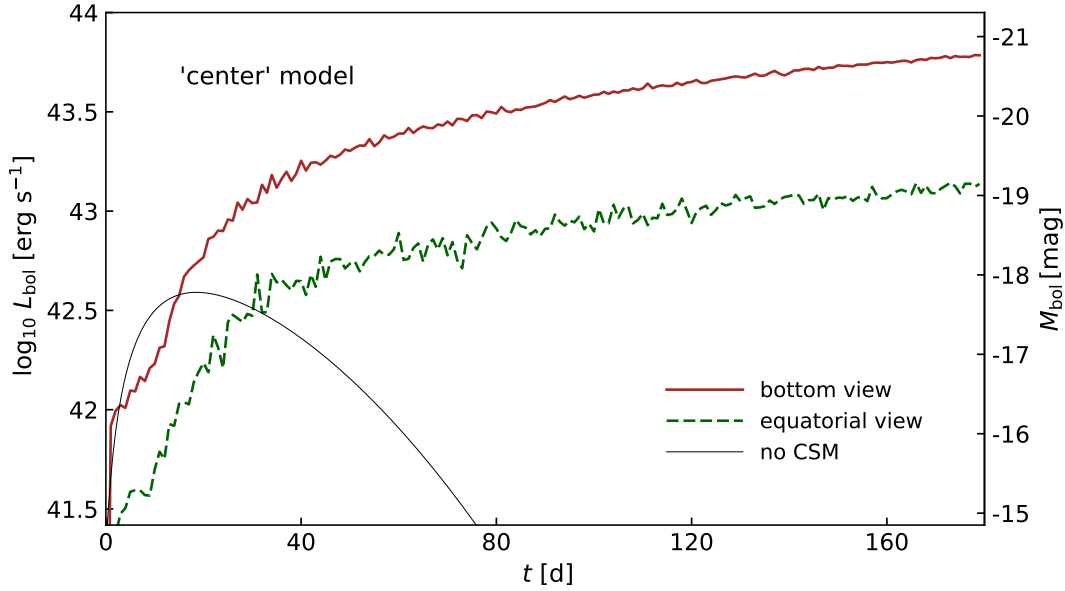


Figure 4.15: logarithm of the bolometric luminosity and absolute bolometric magnitude of the 'center' model over 200 days. Solid black line shows an isolated SN explosion, with no circumstellar material (no CSM).

4.5 Discussion

All the plots in the 'bottom' model from the Castro hydrodynamic simulation exhibit a very strong 'ornament' artifact. It is created due to spherical process being modeled in the Cartesian coordinate system, with the initial spherical part being staircase-like, 'jagged'. The ornament pattern is strongly enhanced in the case of the radiation-hydrodynamic simulation with strong radiative cooling within the optically very thin environment. This could be suppressed by adding more refinement levels, which, however, would drastically increase computational time and necessary storage capacities. Or, possibly, by implementing some more advanced numerical techniques for Cartesian grids (see, e.g., the Immersed boundary method, by Gilmanov and Sotiropoulos (2005)).

The 'bottom' model

Density and temperature plots have a very distinct shock wave running in the front of the main ejecta, which was described in Chapter 2 (Riemann-Sod shock tube). Temperatures rise for up to $\sim 10^5$ K where ejecta interacts with the Galactic accretion disk material. Which, on the other hand, may be deformed by this interaction, so it appears after some time broader at the boundary closer to the SMBH.

Velocity magnitude from the center of the SN to the CD is approximately linear (as shown in the Sedov problem, Figure 4.7), but it grows to $\sim 10^4 \text{ km s}^{-1}$ where the material 'bursts' on the opposite side of the disk.

Light curves for the 'bottom' model have a similar beginning, with the top view gradually rising with the CSM getting hotter and more luminous. The bottom view starts nearly the same, but after first 20 days closely follows the no CSM model. This luminosity profile can be explained by the opacity of SN ejecta, which is blocking the hot and luminous disk material for the first ~ 45 days. After the ejecta expands and gets optically thinner, we get a similar gradual rise, but even higher luminosity.

The 'center' model

Again, the density plot very distinctly exhibits the forward shock, which goes in front of the main ejecta (CD). Temperatures are very high only near the disk midplane, where the interaction of ejecta and gas is the strongest.

Created explosion distorts the disk which becomes broader closer to SMBH. Velocity magnitudes of 'burst out' ejecta from the disk are around $\sim 10^4 \text{ km s}^{-1}$, with approximately linear profile beginning near the center of explosion to the end of the disk.

Even if we could see this as a relatively weak source (due to the very high extinction) in the infrared wavelengths, we still could estimate the 'view' with the help of the light-curve profile. For this reason, such theoretical studies may be useful in order to better understand the processes that occur near the Galactic Center, which are hard to measure and observe with the standard or usual methods.

Conclusions

This work discussed some models of SN interactions near the Galactic Center. Using the SNEC code for the one-dimensional post-breakout SN profile, we used the Castro code for radiation-hydrodynamics calculation. Simulated models and subsequently calculated light curves basically fit with proposed models and solutions in Kurfürst (2010), Kurfürst et al. (2020), and Alsabti and Murdin (2017). Hydrodynamical models show some similarities with the Riemann-Sod shock tube and the Sedov blast-wave problems, with approximately radial profiles of magnitude of the velocity and distinct CD and forward shock waves. Due to the SN-disk interactions, temperatures rise up to $\sim 10^5$ K in certain zones of interaction. Light curves, which were calculated with Sedona code, exhibit different features for different problem morphologies. The 'bottom' model had a big difference in the top and bottom views, with the latter closely following the isolated SN (no CSM) profile in the early phase. After ~ 50 days, the bottom view rises and the luminosity becomes higher than the top view one, which can be explained by the opacity of the expanding ejecta, which partly swallows the hot and luminous SN-disk interactions. The 'center' model has roughly monotonic light curves, with significantly higher statistical noise in equatorial view, due to the lack of photon packets passing in the longitudinal direction of the Galactic disk.

The performed models may serve as a basis for following, more advanced work inclusion of longer computational time of interactions. It will be also highly desirable to calculate the spectral and polarization signatures of the interaction process which the Sedona multi-dimensional code is capable of. However, such calculations are currently beyond the scope of the thesis and will be the subject of the future work.

Bibliography

- A. Almgren, M. B. Sazo, J. Bell, A. Harpole, M. Katz, J. Sexton, D. Willcox, W. Zhang, and M. Zingale. Castro: A massively parallel compressible astrophysics simulation code. *Journal of Open Source Software*, 5(54):2513, 2020. doi: 10.21105/joss.02513. URL <https://doi.org/10.21105/joss.02513>.
- A. W. Alsabti and P. Murdin. *Handbook of Supernovae*. 2017. doi: 10.1007/978-3-319-21846-5.
- B. Barbuy, C. Chiappini, and O. Gerhard. Chemodynamical History of the Galactic Bulge. *ARA&A*, 56:223–276, Sept. 2018. doi: 10.1146/annurev-astro-081817-051826.
- C. Battersby, D. L. Walker, A. Barnes, A. Ginsburg, D. Lipman, D. Albolani, H. P. Hatchfield, J. Bally, S. C. O. Glover, J. D. Henshaw, K. Immer, R. S. Klessen, S. N. Longmore, E. A. C. Mills, S. Molinari, R. Smith, M. C. Sormani, R. G. Tress, and Q. Zhang. 3-D CMZ I: Central Molecular Zone Overview. *arXiv e-prints*, art. arXiv:2410.17334, Oct. 2024. doi: 10.48550/arXiv.2410.17334.
- M. J. Berger and J. Olinger. Adaptive Mesh Refinement for Hyperbolic Partial Differential Equations. *Journal of Computational Physics*, 53(3):484–512, Mar. 1984. doi: 10.1016/0021-9991(84)90073-1.
- A. Blaauw, C. S. Gum, J. L. Pawsey, and G. Westerhout. The new I. A. U. system of galactic coordinates (1958 revision). *MNRAS*, 121:123, Jan. 1960. doi: 10.1093/mnras/121.2.123.
- B. W. Carroll and D. A. Ostlie. *An introduction to modern astrophysics, Second Edition*. 2017.
- A. Ciurlo and M. R. Morris. Sagittarius A* – The Milky Way Supermassive Black Hole. *arXiv e-prints*, art. arXiv:2503.20081, Mar. 2025. doi: 10.48550/arXiv.2503.20081.
- A. Feldmeier-Krause, N. Neumayer, R. Schödel, A. Seth, M. Hilker, P. T. de Zeeuw, H. Kuntschner, C. J. Walcher, N. Lützgendorf, and M. Kissler-Patig. KMOS view of the

Galactic centre. I. Young stars are centrally concentrated. *A&A*, 584:A2, Dec. 2015. doi: 10.1051/0004-6361/201526336.

E. E. E. Gall, J. Polshaw, R. Kotak, A. Jerkstrand, B. Leibundgut, D. Rabinowitz, J. Sollerman, M. Sullivan, S. J. Smartt, J. P. Anderson, S. Benetti, C. Baltay, U. Feindt, M. Fraser, S. González-Gaitán, C. Inserra, K. Maguire, R. McKinnon, S. Valenti, and D. Young. A comparative study of Type II-P and II-L supernova rise times as exemplified by the case of LSQ13cuw. *A&AP*, 582:A3, Oct. 2015. doi: 10.1051/0004-6361/201525868.

A. Gilmanov and F. Sotiropoulos. A hybrid Cartesian/immersed boundary method for simulating flows with 3D, geometrically complex, moving bodies. *Journal of Computational Physics*, 207(2):457–492, Aug. 2005. doi: 10.1016/j.jcp.2005.01.020.

GRAVITY Collaboration, R. Abuter, A. Amorim, M. Bauböck, J. P. Berger, H. Bonnet, W. Brandner, Y. Clénet, V. Coudé Du Foresto, P. T. de Zeeuw, J. Dexter, G. Duvert, A. Eckart, F. Eisenhauer, N. M. Förster Schreiber, P. Garcia, F. Gao, E. Gendron, R. Genzel, O. Gerhard, S. Gillessen, M. Habibi, X. Haubois, T. Henning, S. Hippler, M. Horrobin, A. Jiménez-Rosales, L. Jocou, P. Kervella, S. Lacour, V. Lapeyrère, J. B. Le Bouquin, P. Léna, T. Ott, T. Paumard, K. Perraut, G. Perrin, O. Pfuhl, S. Rabien, G. Rodriguez Coira, G. Rousset, S. Scheithauer, A. Sternberg, O. Straub, C. Straubmeier, E. Sturm, L. J. Tacconi, F. Vincent, S. von Fellenberg, I. Waisberg, F. Widmann, E. Wieprecht, E. Wieszorrek, J. Woillez, and S. Yazici. A geometric distance measurement to the Galactic center black hole with 0.3% uncertainty. *A&AP*, 625:L10, May 2019. doi: 10.1051/0004-6361/201935656.

J. D. Henshaw, A. T. Barnes, C. Battersby, A. Ginsburg, M. C. Sormani, and D. L. Walker. Star Formation in the Central Molecular Zone of the Milky Way. In S. Inutsuka, Y. Aikawa, T. Muto, K. Tomida, and M. Tamura, editors, *Protostars and Planets VII*, volume 534 of *Astronomical Society of the Pacific Conference Series*, page 83, July 2023. doi: 10.48550/arXiv.2203.11223.

M. P. Katz, M. Zingale, A. C. Calder, F. D. Swesty, A. S. Almgren, and W. Zhang. White Dwarf Mergers on Adaptive Meshes. I. Methodology and Code Verification. *ApJ*, 819:94, Mar. 2016. doi: 10.3847/0004-637X/819/2/94.

M. R. Krumholz, R. I. Klein, C. F. McKee, and J. Bolstad. Equations and Algorithms for Mixed-

- frame Flux-limited Diffusion Radiation Hydrodynamics. *ApJ*, 667(1):626–643, Sept. 2007. doi: 10.1086/520791.
- P. Kurfürst. Models of hot star decretion disks. *arXiv e-prints*, art. arXiv:2402.17575, Feb. 2015. doi: 10.48550/arXiv.2402.17575.
- P. Kurfürst, O. Pejcha, and J. Krtićka. Supernova explosions interacting with aspherical circumstellar material: implications for light curves, spectral line profiles, and polarization. *A&AP*, 642:A214, Oct. 2020. doi: 10.1051/0004-6361/202039073.
- P. Kurfürst, M. Zajaček, N. Werner, and J. Krtićka. Red giant - jet collisions in galactic nuclei I: 3D hydrodynamical model of a few stellar orbits. *arXiv e-prints*, art. arXiv:2409.17773, Sept. 2024. doi: 10.48550/arXiv.2409.17773.
- P. Kurfürst. *ASTROFYZIKA SUPERNOV, Diplomová práce*. 2010.
- C. D. Levermore and G. C. Pomraning. A flux-limited diffusion theory. *ApJ*, 248:321–334, Aug. 1981. doi: 10.1086/159157.
- A. Mezzacappa and S. W. Bruenn. A Numerical Method for Solving the Neutrino Boltzmann Equation Coupled to Spherically Symmetric Stellar Core Collapse. *ApJ*, 405:669, Mar. 1993. doi: 10.1086/172395.
- V. Morozova, A. L. Piro, M. Renzo, C. D. Ott, D. Clausen, S. M. Couch, J. Ellis, and L. F. Roberts. Light Curves of Core-collapse Supernovae with Substantial Mass Loss Using the New Open-source SuperNova Explosion Code (SNEC). *ApJ*, 814(1):63, Nov. 2015. doi: 10.1088/0004-637X/814/1/63.
- E. M. Murchikova, E. S. Phinney, A. Pancoast, and R. D. Blandford. A cool accretion disk around the Galactic Centre black hole. *Nature*, 570(7759):83–86, June 2019. doi: 10.1038/s41586-019-1242-z.
- N. Neumayer, A. Seth, and T. Böker. Nuclear star clusters. *A&ApR*, 28(1):4, July 2020. doi: 10.1007/s00159-020-00125-0.
- B. Paczynski. Models of X-ray bursters with radius expansion. *ApJ*, 267:315–321, Apr. 1983. doi: 10.1086/160870.

- B. Paxton, L. Bildsten, A. Dotter, F. Herwig, P. Lesaffre, and F. Timmes. Modules for Experiments in Stellar Astrophysics (MESA). *ApJS*, 192(1):3, Jan. 2011. doi: 10.1088/0067-0049/192/1/3.
- M. Portail, C. Wegg, O. Gerhard, and I. Martinez-Valpuesta. Made-to-measure models of the Galactic box/peanut bulge: stellar and total mass in the bulge region. *MNRAS*, 448(1): 713–731, Mar. 2015. doi: 10.1093/mnras/stv058.
- N. Roth and D. Kasen. Monte Carlo Radiation-Hydrodynamics With Implicit Methods. *ApJS*, 217(1):9, Mar. 2015. doi: 10.1088/0067-0049/217/1/9.
- G. B. Rybicki and A. P. Lightman. *Radiative Processes in Astrophysics*. 1986.
- R. H. Sanders and G. T. Wrixon. The Center of the Galaxy. *Scientific American*, 230(4):66–77, Apr. 1974. doi: 10.1038/scientificamerican0474-66.
- R. Schödel, D. Merritt, and A. Eckart. The nuclear star cluster of the Milky Way: proper motions and mass. *A&AP*, 502(1):91–111, July 2009. doi: 10.1051/0004-6361/200810922.
- R. Schödel, A. Feldmeier, N. Neumayer, L. Meyer, and S. Yelda. The nuclear cluster of the Milky Way: our primary testbed for the interaction of a dense star cluster with a massive black hole. *Classical and Quantum Gravity*, 31(24):244007, Dec. 2014. doi: 10.1088/0264-9381/31/24/244007.
- H. Shapley. Studies based on the colors and magnitudes in stellar clusters. VII. The distances, distribution in space, and dimensions of 69 globular clusters. *ApJ*, 48:154–181, Oct. 1918. doi: 10.1086/142423.
- N. Smith, R. Chornock, W. Li, M. Ganeshalingam, J. M. Silverman, R. J. Foley, A. V. Filippenko, and A. J. Barth. SN 2006tf: Precursor Eruptions and the Optically Thick Regime of Extremely Luminous Type II_n Supernovae. *ApJ*, 686(1):467–484, Oct. 2008. doi: 10.1086/591021.
- G. A. Sod. Review. A Survey of Several Finite Difference Methods for Systems of Nonlinear Hyperbolic Conservation Laws. *Journal of Computational Physics*, 27(1):1–31, Apr. 1978. doi: 10.1016/0021-9991(78)90023-2.

- J. Von Neumann and R. D. Richtmyer. A Method for the Numerical Calculation of Hydrodynamic Shocks. *Journal of Applied Physics*, 21(3):232–237, Mar. 1950. doi: 10.1063/1.1699639.
- C. J. Walcher, T. Böker, S. Charlot, L. C. Ho, H. W. Rix, J. Rossa, J. C. Shields, and R. P. van der Marel. Stellar Populations in the Nuclei of Late-Type Spiral Galaxies. *ApJ*, 649(2):692–708, Oct. 2006. doi: 10.1086/505166.
- W. Zhang, L. Howell, A. Almgren, A. Burrows, and J. Bell. CASTRO: A New Compressible Astrophysical Solver. II. Gray Radiation Hydrodynamics. *ApJS*, 196:20, Oct. 2011. doi: 10.1088/0067-0049/196/2/20.
- W. Zhang, L. Howell, A. Almgren, A. Burrows, J. Dolence, and J. Bell. CASTRO: A New Compressible Astrophysical Solver. III. Multigroup Radiation Hydrodynamics. *ApJS*, 204:7, Jan. 2013. doi: 10.1088/0067-0049/204/1/7.
- W. Zhang, A. Almgren, V. Beckner, J. Bell, J. Blaschke, C. Chan, M. Day, B. Friesen, K. Gott, D. Graves, M. P. Katz, A. Myers, T. Nguyen, A. Nonaka, M. Rosso, S. Williams, and M. Zingale. Amrex: a framework for block-structured adaptive mesh refinement. *Journal of Open Source Software*, 4(37):1370, 2019. doi: 10.21105/joss.01370. URL <https://doi.org/10.21105/joss.01370>.